Proposal for
Drell-Yan Measurements of Nucleon and Nuclear Structure with the FNAL Main Injector

L. D. Isenhower, M. E. Sadler
Abilene Christian University, Abilene, TX 79699

J. Arrington, D. F. Geesaman (Co-Spokesperson), R. J. Holt, H. E. Jackson,
P. E. Reimer (Co-Spokesperson), D. H. Potterveld
Argonne National Laboratory, Argonne IL 60439

C. N. Brown
Fermi National Accelerator Laboratory, Batavia, IL 60510

G. T. Garvey, M. J. Leitch, P. L. McGaughey, J.-C. Peng, R. S. Towell
Los Alamos National Laboratory, Los Alamos, NM 87545

R. Gilman, C. Glashausser, X. Jiang, R. Ransome, S. Strauch
Rutgers University, Rutgers, NJ 08544

C. A. Gagliardi, R. E. Tribble, M. A. Vasiliev
Texas A & M University, College Station, TX 77843-3366

D. D. Koetke
Valparaiso University, Valparaiso, IN 46383

(The P906 Collaboration)

April 1, 2001

Abstract

We propose measuring the fractional momentum (x) dependence of the ratio of the anti-down to anti-up quark distributions in the proton, $\bar{d}(x)/\bar{u}(x)$, using proton induced Drell-Yan reactions at 120 GeV. Recent measurements by FNAL E866 unexpectedly show considerable x dependence in this ratio for $x > 0.2$. A lower energy primary proton beam from the Main Injector makes it possible to extend the E866 measurements to larger x with much higher precision. The apparatus will also be used with nuclear targets to measure parton energy loss and modifications to anti-quark distributions in nuclear targets at large x ($x > 0.2$).

Contents

1 Introduction

While proton structure functions have been measured in deep inelastic scattering over five orders of magnitude in both the fractional momentum of the parton, x, and the virtuality of the incident photon, Q^2, the factorizable, non-perturbative parton distributions must be determined by phenomenological fits [1, 2, 3, 4, 5]. Each time new data have tested underlying assumptions of the phenomenology, the phenomenology has been found wanting. For example, no known symmetry requires the equality of the anti-down [$\bar{d}_p(x)$] and anti-up [$\bar{u}_p(x)$] quark distributions in the proton, but, until 1991, this was a common assumption. Following the NMC observation [6] that the integral of $\bar{d}_p(x) - \bar{u}_p(x)$ is non-zero, NA51 [7] used the Drell-Yan process to confirm this difference. E866 [8, 9, 10] recently measured the x dependence of $\bar{d}_p(x)/\bar{u}_p(x)$ and $\bar{d}_p(x) - \bar{u}_p(x)$ from $0.015 < x < 0.35$. The E866 results for $\bar{d}_p(x)/\bar{u}_p(x)$ are shown in Fig. 1 along with the NA51 result and the various parton distribution fits illustrate the impact of inclusion of the E866 data.

Fundamentally, the nucleon structure functions are non-perturbative manifestations of Quantum Chromodynamics. While perturbative QCD quantitatively describes the Q^2 evolution of the parton distributions, the origins of the parton distributions themselves have not proved amenable to QCD treatment, although many *models* exist in the literature. Measurements of those distributions that are poorly determined provide vital information on nucleon structure which is used to constrain and refine the phenomenology. For example, in the MRST [4] and CTEQ5 [2] global fits incorporating the E866 results, both the sea and valence distributions differ substantially from previous parameterizations.

We propose making precise measurements of proton-induced Drell-Yan cross sections on hydrogen and deuterium. From these measurements we will determine $\bar{d}_p(x)/\bar{u}_p(x)$ for $0.1 < x < 0.45$. The measurements on deuterium are also directly sensitive to the antiquark sea, $\bar{d}_p(x) + \bar{u}_p(x)$, over this same range[1]. We further propose measuring proton-induced Drell-Yan cross sections on nuclear targets. Our present knowledge of the flavor dependence of the nuclear parton distributions limits the understanding of the nuclear dependences that have been observed (e.g. [11]). These nuclear measurements also provide a direct comparison with neutrino data on nuclear targets which are currently used to measure $\bar{d}(x) + \bar{u}(x)$. The results of these measurements will also have implications in other areas. For example, in proton-proton collider experiments the highest energy scales are achieved via $q\bar{q}$ annihilation of large x partons. The ratio of $\bar{d}(x)/\bar{u}(x)$ results from a competition between non-perturbative and QCD gluon splitting contributions and high x results may provide constraints on the gluon distributions at high x which evolve into the antiquark distributions needed at high mass scales.

The design of the experimental apparatus relies heavily on our previous experience in E605, E772, E789 and E866. Much of the detector hardware already exists and was used in these previous experiments or in E871. Because of the lower energy, however, it will be necessary to fabricate coils for a new magnet.

2 Discussion of Physics

To lowest order, the Drell-Yan process, virtual photon production in hadron-hadron collisions, depends on the product of quark and antiquark distributions in the beam and target

[1]From here on, unless otherwise needed for clarity, $\bar{d}(x)$ and $\bar{u}(x)$ will refer to the distributions in the proton and the subscript p will be dropped.

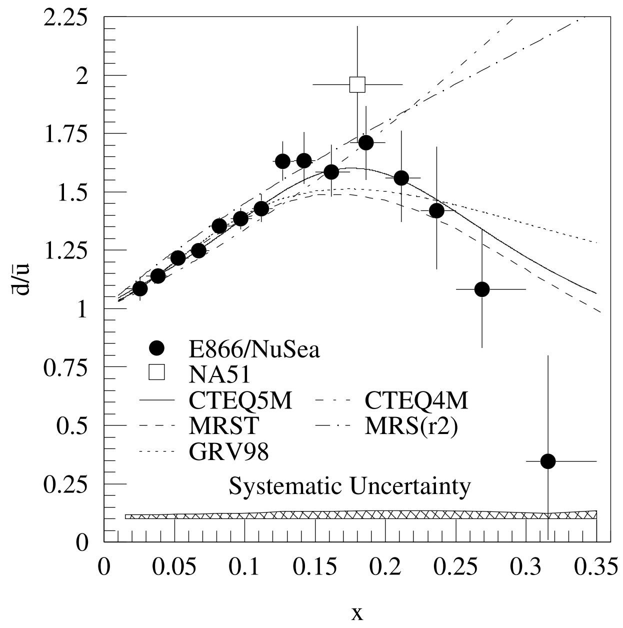

Figure 1: FNAL E866 results [10] for the x-dependence of the ratio $\bar{d}_p(x)/\bar{u}_p(x)$ of the proton at a mass scale of 7.35 GeV. The square is the NA51 result at a mass scale of 5.2 GeV [7]. Also shown are parameterizations of this ratio from CTEQ4M [1] and MRS(r2) [3] prior to the FNAL E866 results and parameterizations from CTEQ5M [2], MRST [4] and GRV98 [5] which have included the E866 data in the fitting procedure.

as:

$$\frac{d^2\sigma}{dx_1 dx_2} = \frac{4\pi\alpha^2}{9 s x_1 x_2} \sum_i e_i^2 \left[q_i^b(x_1, Q^2)\bar{q}_i^t(x_2, Q^2) + \bar{q}_i^b(x_1, Q^2) q_i^t(x_2, Q^2) \right] \tag{1}$$

where the superscripts b (t) label the beam (target) and the sum is over all quark flavors (u, d, s, c, b, t). The fraction of the longitudinal momentum of the beam carried by the quark from the beam is x_1 and similarly x_2 is the fraction of the longitudinal momentum of the target carried by the quark from the target. The squared total energy of the beam-target system is $s = 2m_t * E_b + m_b^2 + m_t^2$ with E_b the energy of the beam hadron and m_b and m_t the rest masses of the beam and target hadron respectively. In the case of nuclear targets, we will assume the reaction takes place on a component nucleon, $m_t = M_n$, where M_n is the nucleon mass, and the momentum fraction is A (the number of nucleons) times the fraction of the momentum of the quark compared with the entire nucleus. The convention that $c = 1$ is used throughout the text.

The kinematics of the virtual photon—longitudinal center of mass momentum $p_{||}^{\gamma}$, transverse momentum p_T^{γ} and mass M_γ—are determined by measuring the two-muon decay of the virtual photon. These quantities determine the momentum fractions of the two quarks:

$$x_F = \frac{p_{||}^{\gamma}}{p_{||}^{\gamma,\max}} \approx x_1 - x_2 \tag{2}$$

$$x_1 x_2 s \approx M_\gamma^2 \tag{3}$$

where $p_{||}^{\gamma,\max}$ is the kinematic maximum value it can have.

In the kinematical region with $x_F > 0$ and x_1 large, the reaction is dominated by valence quarks from the beam annihilating with antiquarks from the target, giving sensitivity to the target antiquark distributions. In this limit the contribution from the second term in Eq. 1 is small. With a proton beam the first term is dominated by the $u(x_1)$ distribution of the proton. Under these circumstances, the ratio of the cross sections for two different targets, X and Y, which have A_X and A_Y nucleons is approximately the ratio of the $\bar{u}(x)$ distributions:

$$\frac{\frac{1}{A_X}\left(\frac{d\sigma^X}{dx_1 dx_2}\right)}{\frac{1}{A_Y}\left(\frac{d\sigma^Y}{dx_1 dx_2}\right)} \approx \left.\frac{\bar{u}^X(x_2)}{\bar{u}^Y(x_2)}\right|_{x_1 \gg x_2}. \tag{4}$$

In this relation the cross sections are defined per nucleus while the parton distributions are conventionally defined per nucleon.

Equation 4 demonstrates the power of Drell-Yan experiments in determining relative antiquark distributions. We wish to extend the measurements made by E866 to relatively large x_2 where the antiquark distributions are small. Beams from the 120 GeV FNAL Main Injector have two primary advantages compared with previous 800 GeV measurements:

- For fixed x_1 and x_2 the cross section is proportional to $1/E_b$, where E_b is the incident beam energy, as shown in Eq. 1. A Main Injector experiment will have a factor of approximately 7 times larger cross sections compared with experiments with the 800 GeV Tevatron extracted beam.

- Practical limitations in the acceptable luminosity for these experiments are radiation protection limits and the single muon rates in the detectors. To the extent that the radiation dose scales as beam power, one can take approximately 7 times the luminosity for the same beam power at 120 GeV relative to 800 GeV. In E866 at 800 GeV, J/ψ events from the beam dump were a significant contribution to the muon singles rates. At 120 GeV the total J/ψ production cross sections fall by an order of magnitude when compared with 800 GeV.

We expect that the combination of these effects will allow a factor of 50 improvement in the number of recorded events at high x_2 compared with E866 or E772.

2.1 Parton Distributions: $\bar{d}(x)/\bar{u}(x)$ of the Proton

E866 and NA51 used measurements of the ratio of the Drell-Yan cross sections on deuterium and hydrogen to determine the ratio of $\bar{d}(x)/\bar{u}(x)$ on the proton by assuming the deuterium cross section is the sum of the proton and neutron cross sections and using charge symmetry to equate $\bar{d}_p$ to $\bar{u}_n$. When the antiquarks in the beam and the strange and heavier antiquarks in the target are ignored:

$$\left.\frac{\sigma^{pd}}{2\sigma^{pp}}\right|_{x_1 >> x_2} \approx \frac{1}{2}\left[\frac{1+\frac{d(x_1)}{4u(x_1)}}{1+\frac{d(x_1)\bar{d}(x_2)}{4u(x_1)\bar{u}(x_2)}}\right]\left[1+\frac{\bar{d}(x_2)}{\bar{u}(x_2)}\right]. \tag{5}$$

Observing that $d(x) \ll 4u(x)$, this expression simplifies even further to

$$\left.\frac{\sigma^{pd}}{2\sigma^{pp}}\right|_{x_1 >> x_2} \approx \frac{1}{2}\left[1+\frac{\bar{d}(x_2)}{\bar{u}(x_2)}\right]. \tag{6}$$

While this expression illustrates the sensitivity of the experimental ratio to $\bar{d}(x)/\bar{u}(x)$, the E866 extraction of $\bar{d}(x)/\bar{u}(x)$ was performed using Eq. 1 (and verified with a full next-to-leading order calculation). The CTEQ5M distributions were used for the valence quark distributions, the sum $\bar{d}(x) + \bar{u}(x)$, and the heavier sea quark distributions in Eq. 1. The resulting $\bar{d}(x)/\bar{u}(x)$ distributions showed little variation if the MRS(R2), MRST or CTEQ4M parton distributions were used for these values.

2.1.1 Origins of the Nucleon Sea

While providing direct input to the parton distribution fits, the ultimate impact of our experiment will be to provide a better understanding on the physical mechanism which generates the sea of the proton.

The $\bar{d}(x) - \bar{u}(x)$ difference, shown in Fig. 2, is a pure flavor non-singlet quantity: its integral is Q^2 independent [12] and its Q^2 evolution at leading order does not depend on the gluon distribution of the proton. Early expectations were that Pauli blocking due to the extra valence u quark in the proton would lead to a suppression of $g \to u\bar{u}$ which would contribute significantly to differences in the light sea [13]. These expectations were not, however, borne out by calculations [14, 15] (though this point is still debated in the literature [16]). In perturbative QCD, differences between the $\bar{d}(x)$ and $\bar{u}(x)$ distributions arise only at second order and are calculated to be very small [14]. The large differences seen in Figs. 1 and 2 must be non-perturbative in nature and are likely explained in terms of collective degrees of freedom of QCD at low energy.

There are three significant non-perturbative approaches which can accommodate large $\bar{d}(x) - \bar{u}(x)$ differences: (1) hadronic models of the meson cloud of the nucleon, (2) chiral quark models which couple mesons directly to constituent quarks and (3) instanton models. Figure 2 illustrates calculations for representative examples of each of these models. An intriguing feature is that in each of these models the flavor and spin distributions of the proton are intimately linked. As these non-perturbative models are considered, it is important to remember that they must be combined with perturbative sources to generate the entire quark sea of the proton.

The pion cloud model has a tantalizing simplicity and does explain basic features of the data. A proton wave function containing sizable virtual $|n\pi^+\rangle$ Fock states will have an excess of $\bar{d}$-quarks from the valence quarks in the π^+. The difficulty in this approach is finding justification to truncate the hadronic expansion [17]. Most calculations include contributions for $|N\pi\rangle$ and $|\Delta\pi\rangle$ states (*e.g.* Ref. [18]). The pion-nucleon and pion-delta coupling constants ($g_{\pi NN}$ and $g_{\pi N\Delta}$) are well known, so the primary difference among calculations is the treatment of the πNN and $\pi N\Delta$ vertex factors. Using "not unreasonable" vertex functions (dipole vertex functions with cut offs, Λ, of $\Lambda_{\pi NN} = 1.0$ GeV and $\Lambda_{\pi N\Delta} = 0.8$ GeV) good agreement with the data [9] is found as show in the solid curve of Fig. 2. The resulting probabilities for the $|N\pi\rangle$ and $|\Delta\pi\rangle$ admixture lead to a prediction for the difference in total spin carried by the u quarks (Δu) and the d quarks (Δd), $\Delta u - \Delta d = G_A$ of ≈ 1.5 [9], providing part of the reduction from the quark model value of 5/3.

Chiral field theories suggest that the relevant degrees of freedom are constituent quarks, gluons and Goldstone bosons. Processes such as $u \to d\pi^+$ and $d \to u\pi^-$ generate a flavor asymmetry in the sea simply because there are more up than down quarks in the proton. Two predictions of $\bar{d}(x) - \bar{u}(x)$ from chiral models are shown in Fig. 2 at the dotted and dot-dashed curves. Clearly the model of Szczurek *et al.* [19] is too soft. The chiral quark-soliton

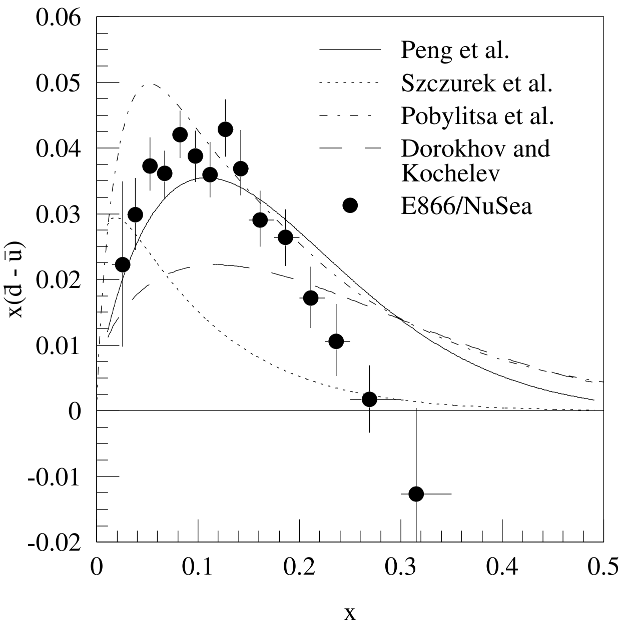

Figure 2: FNAL E866 results [8, 9, 10] for the x-dependence of $x\left[\bar{d}(x)-\bar{u}(x)\right]$ of the proton at a mass scale of 7.35 GeV. The curves represent four model calculations of $x\left[\bar{d}(x)-\bar{u}(x)\right]$. The solid curve is a meson-cloud model calculation including nucleons, deltas and pions [9]. The dotted and dot-dashed curves are a chiral quark models [19] and the long-dashed curve is an instanton inspired parameterization [22].

model of Pobylitsa *et al.* [20] better reproduces the measured $x\left[\bar{d}(x)-\bar{u}(x)\right]$ distribution for $x > 0.08$, but overestimates the asymmetry at small x.

Instanton effective Lagrangians imply coupling at the tree level between instantons and the valence quarks which leads to a $\bar{d}(x)-\bar{u}(x)$ difference. This raises the intriguing possibility that Drell-Yan measurements could provide experimental information on these theoretically very useful but seemingly experimentally inaccessible constructs. Within the framework of the t'Hooft SU(2) effective Lagrangian [21] (which is of the form $\bar{u}_R u_L \bar{d}_R d_L + \bar{u}_L u_R \bar{d}_L d_R$ where the subscripts R and L label the quark helicity) the u quarks generate a $\bar{d}d$ sea and the helicity of the valence quarks is screened [22]. (A flavor SU(3) Lagrangian would also generate $s\bar{s}$ pairs.) Dorokhov and Kochelev fit the NMC measurement of the $\bar{d}(x)-\bar{u}(x)$ integral to a form parameterized to have the expected asymptotes which is shown as the long-dashed curve on Fig. 2. The $\bar{d}(x)-\bar{u}(x)$ difference observed by E866 does not show the transverse momentum (p_T) dependence expected in Ref. [22], however. One set of predictions is the relations between the instanton contributions (subscript I in Eq. 7) of the spin and flavor matrix elements, for example:

$$\bar{d}_I(x)-\bar{u}_I(x)=\frac{3}{5}\left[\Delta u_I(x)-\Delta d_I(x)\right] \tag{7}$$

It is interesting to note that while this approach gives a reduction in the total spin carried by the quarks in the nucleon, it implies an increase in $\Delta u_I(x)-\Delta d_I(x)$ while in the other models an increase in the flavor asymmetry causes a decrease in $\Delta u(x)-\Delta d(x)$.

As mentioned earlier, none of these models consistently incorporate the flavor symmetric

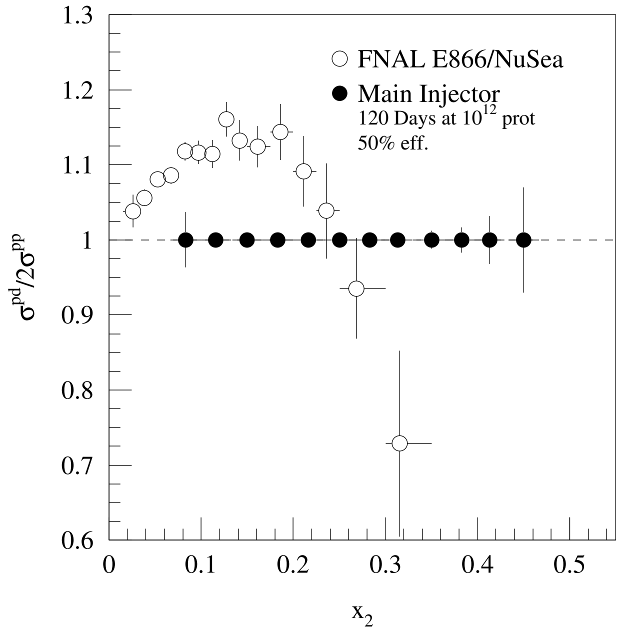

Figure 3: FNAL E866 results[8, 10] for the x-dependence of the ratio of $\sigma^{pd}/2\sigma^{pp}$. The statistical uncertainties expected for the measurement proposed here are shown as the error bars on the solid circles (which are arbitrarily plotted at 1.0). The systematic errors are estimated to be less than 1%.

sea and consequently all substantially over predict the ratio of $\bar{d}(x)/\bar{u}(x)$ for x >0.23. Unfortunately the statistical uncertainty on the E866 data becomes large in this region. The pion models tend to level off at a predicted $\bar{d}(x)/\bar{u}(x)$ between 1.5 and 5 (depending on the baryons and mesons included in the calculations) until $x > 0.5$ where the ratio begins to decrease slowly to unity. The instanton model predicts a ratio of $\bar{d}(x)/\bar{u}(x) \approx 4$ at high x. One possible interpretation of the E886 results is the perturbative gluon mechanism begins to re-establish its dominance over the non-perturbative mechanisms at a lower value of x than previously expected. Note that the gluon distribution at high x changed considerably from MRS(r2) [3] to MRST [4] with a change in the treatment of the fixed target prompt photon data. In addition, recent collider inclusive jet cross sections suggest a stronger gluon content to the proton than is present in the parameterizations [23].

The expected statistical precision with which one can measure the ratio $\sigma^{pd}/2\sigma^{pp}$ in an experiment at the Main Injector is shown by the error bars on the solid points in Fig. 3 along with the E866 measurements. It is apparent that a high luminosity Main Injector experiment can extend the x range of our knowledge of $\bar{d}(x)/\bar{u}(x)$ up to $x \approx 0.45$.

2.1.2 Influence on Parton Distribution Functions

As can be seen by comparing the $\bar{d}(x)/\bar{u}(x)$ curves shown in Fig. 1, the inclusion of the E866 data completely changed the parameterization of the antiquark sea for $x > 0.20$. In determining the anti-quark content of the proton sea, the parton distribution fits have simply parameterized the E866 data with a convenient algebraic form. While the chosen form reproduces the Drell-Yan data well, the statistical uncertainty on the data still allows for up to a 50% variation at $x = 0.3$ compared with only a few percent uncertainty up to $x = 0.4$ in the present proposal, as shown in Fig. 3.

In addition to the Drell-Yan ratio measurement, the absolute Drell-Yan proton-hydrogen and proton-deuterium cross sections will be determined at high x. This measurement is directly sensitive to the magnitude of the anti-quark sea, $\bar{d}(x) + \bar{u}(x)$. Until now, the parton distribution fits obtained sensitivity to the sea distribution at high x from the CCFR neutrino measurements on iron [24], the E605 Drell-Yan measurements on Cu [25], the E772 Drell-Yan measurements on deuterium [26] and the NA51 [7] and E866 [8, 9] Drell-Yan ratio measurements on deuterium and hydrogen. The E605 and E772 measurements will soon be superseded by E866 absolute Drell-Yan cross section results. The magnitude of $(\bar{d} + \bar{u})$ depends on differences between neutrino, anti-neutrino and electron/muon deep inelastic scattering results. The nuclear corrections, which can be different for valence and sea quarks, are a significant uncertainty in these comparisons. One of the primary advances of P906 will be absolute p-p and p-d Drell-Yan cross sections at high x and a precise measurement of the nuclear dependence of the $\bar{u}$ distribution at these x regions.

2.1.3 Interpretability of the Results: QCD factorization

The interpretability of Drell-Yan results as direct measures of the parton distributions is based on the QCD factorization theorems [27, 28]. Bodwin, Brodsky and Lepage [28] give the condition for the minimum beam momentum P_{min} below which initial state QCD interactions become important as:

$$P_{\text{min}} \approx \frac{p_T A^{2/3}}{x_1} \tag{8}$$

A conservative estimate of $\langle p_T^2 \rangle \approx 0.4\ \text{GeV}^2$ (Ref. [28] uses $0.25\ \text{GeV}^2$) yields a typical transverse hadronic scale p_T on the order of 0.6 GeV and a minimum beam momentum of 23 GeV for $x_1 > 0.3$ and a calcium target, comfortably below the 120 GeV considered here.

2.1.4 Competing Measurements of $\bar{d}/\bar{u}$

We see no significant competition for measurements of the flavor dependence of antiquark distributions in this x range. The classes of experiments with potential sensitivity are neutrino deep inelastic scattering (DIS), semi-inclusive deep inelastic scattering (SIDIS), electroweak boson production at pp colliders and other Drell-Yan measurements. We will briefly consider each of these in turn.

CCFR has accumulated significantly more statistics in neutrino and anti-neutrino DIS which will allow a more precise determination of $(\bar{d} + \bar{u})$ but the uncertainties of using a heavy target will remain. On an almost isoscalar target, there is little sensitivity to $(\bar{d} - \bar{u})$.

The flavor dependence of the parton fragmentation functions is used in SIDIS to disentangle the contributions of the different parton distributions. The HERMES collaboration at DESY has used SIDIS to study the flavor dependence of the sea [29]. The HERMES results agree well with the E866 results but have factors of 5 larger error bars, as shown in Fig. 4. SIDIS most directly measures

$$\frac{\bar{d}(x) - \bar{u}(x)}{u(x) - d(x)} = \frac{J(z)\,[1 - r(x,z)] - [1 + r(x,z)]}{J(z)\,[1 - r(x,z)] + [1 + r(x,z)]}, \tag{9}$$

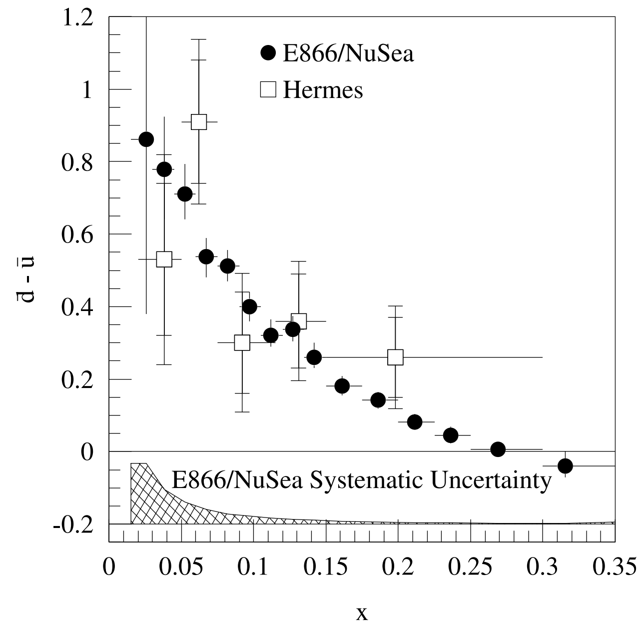

Figure 4: Measurement of $\bar{d}(x) - \bar{u}(x)$ from HERMES [29] compared with the measurements of FNAL E866/NuSea. The inner error bars on the HERMES data points represent the statistical uncertainty while the outer error bars represent the statistical and systematic uncertainty added in quadrature. The uncertainty shown on the E866/NuSea data is statistical, with the systematic uncertainty shown as the band at the bottom.

with

$$r(x,z) = \frac{N_p^{\pi^-} - N_n^{\pi^-}}{N_p^{\pi^+} - N_n^{\pi^+}}. \tag{10}$$

Here, $J(z)$ depends on the fragmentation functions and z is the fraction of the energy of the virtual photon carried by the hadron. At high x where the difference of antiquark distributions is much smaller than the difference of quark distributions, one must measure differences of several comparable size numbers. Additionally, the systematic uncertainty due to the fragmentation physics is also an issue. The experiments which can improve these measurements are HERMES and COMPASS, both of which concentrate on polarized structure function measurements. While HERMES will likely increase their data set by another factor of five in dedicated unpolarized running, they will not be able to extend their x range significantly to higher x. The COMPASS experiment at CERN could do similar semi-inclusive SIDIS measurements. To date they have not proposed dedicated unpolarized running with rapid interchange of pure hydrogen and deuterium targets.

The production of W bosons in p-p collisions does offer sensitivity to the antiquark distributions. At the LHC one only has sensitivity for the x range considered here at the highest rapidities (> 4). However at RHIC higher x values are quite relevant and plans are underway to use the W decay asymmetry in single spin asymmetries to study the antiquark polarization. Since the RHIC detectors have limited kinematic coverage and these events have missing transverse energy, the parton level kinematics of each event are not well determined and one averages over a significant x region. With the antiquark distributions falling rapidly, the lepton asymmetry yields are dominated by lower x values. We have discussed the plans with members of the STAR and PHENIX collaborations at RHIC. They concluded that they will not be sensitive to the antiquark distributions at $x > 0.2$.

In contrast to processes like SIDIS, the Drell-Yan measurement of $\bar{d}/\bar{u}$ has much smaller systematic errors and acceptance corrections. We know of no other planned fixed target Drell-Yan measurements in the near future. In the long term, lower energy, high intensity machines such as the Japanese hadron facility could address this physics. We consider the energy of the main injector to be the optimum combination of reliable interpretation and attainable precision.

Experts like James Sterling [30] have given their strongest support to our proposal as the best way to measure the flavor dependence of the antiquark distributions at high x. Again we see no serious competition for this experiment in the near future.

2.2 Partonic Energy Loss

Parton energy loss is a fundamental process within QCD that has significant impact on the physics of relativistic heavy-ion collisions. The magnitude of the initial energy loss in the heavy-ion collision determines the ultimate density that is achieved. Furthermore, anomalous energy loss of fast partons ("jet quenching") has been identified as a possible signature for the creation of a quark-gluon plasma. Preliminary results on the p_T dependence of π^0 production in 65 GeV/nucleon Au-Au collisions at RHIC were presented by the PHENIX collaboration at the recent Quark Matter conference [31]. They were interpreted as providing clear evidence for parton energy loss in central collisions, although they only appear to require an energy loss of approximately 0.25 GeV/fm, which is less than had been anticipated.

The Drell-Yan process provides an excellent means to study the interactions of fast partons traversing cold nuclei since the dimuon in the final state does not interact strongly with the partons in the medium. Thus, it can be used to estimate the energy loss of fast quarks in nuclear matter, thereby establishing a baseline for the energy loss that would be expected during a heavy-ion collision even without formation of a quark-gluon plasma. Both E772 [32] and E866 [33] measured the nuclear dependence of Drell-Yan dimuon production in 800 GeV/c p-A collisions, and the E866 results have been analyzed to search for evidence of energy loss of the incident quark as it traversed the nucleus prior to the hard scattering [33].

Three different forms for this energy loss have been proposed, each of which can be expressed in terms of the average change in the incident-parton momentum fraction prior to the collision, Δx_1, as a function of target atomic mass (A). Gavin and Milana [34] adopted a form

$$\Delta x_1 = -\kappa_1 \, x_1 \, A^{1/3}, \tag{11}$$

based on an analogy to the transverse spin asymmetry in direct photon production. Brodsky and Hoyer [35] used an analogy to the photon bremsstrahlung process to obtain a form for gluon radiation, leading to an initial-parton energy loss

$$\Delta x_1 \approx -\frac{\kappa_2}{s} A^{1/3}. \tag{12}$$

They also noted that elastic scattering should make a similar contribution to the energy loss. The formulation developed by Brodsky and Hoyer was extended by Baier *et al.* [36].

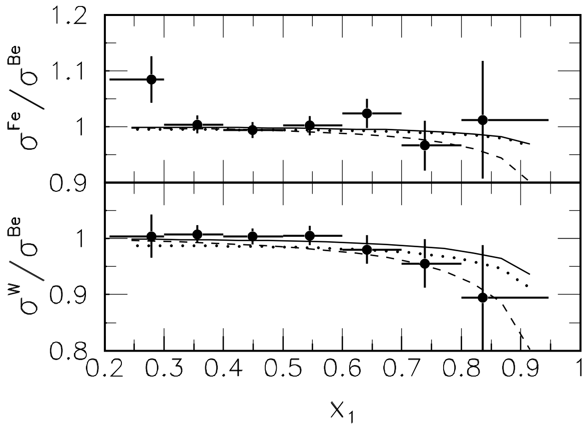

Figure 5: E866 ratios of the Drell-Yan cross section per nucleon versus x_1 for Fe/Be (upper panel) and W/Be (lower panel), corrected for shadowing [33]. The solid curves are the best fit using the energy loss form in Eq. 11, and the dashed curves show the one standard deviation upper limits. The dotted curves show the one standard deviation upper limits using the energy loss form in Eq. 13. The upper limit curves using the energy loss form in Eq. 12 are essentially identical to those using the form in Eq. 13.

They found that the energy loss of sufficiently energetic partons depends on a characteristic length and the broadening of the squared transverse momentum of the parton. For finite nuclei, both factors vary as $A^{1/3}$, so Baier *et al.* predict

$$\Delta x_1 \approx -\frac{\kappa_3}{s} A^{2/3}. \tag{13}$$

In each of these three equations, κ is a constant that sets the overall scale of the energy loss.

In all three cases, the signature for incident-parton energy loss is a modification of the Drell-Yan cross section per nucleon on a heavy nucleus as a function of x_1. However, the E866 nuclear dependence data were taken at relatively small x_2 ($\langle x_2 \rangle = 0.038$), where deep-inelastic scattering experiments show clear evidence for nuclear shadowing. In addition, the Drell-Yan acceptance in E866 introduced a strong anti-correlation between x_1 and x_2. Thus, it was essential to correct the data for the effects of nuclear shadowing. The EKS98 shadowing parameterization [37] was designed to fit the observed nuclear dependence of deep-inelastic scattering over a broad range of Bjorken-x and the nuclear dependence of Drell-Yan scattering observed by E772 at $x_2 > 0.08$, while simultaneously conserving baryon number and momentum. It gives a very good description of the nuclear dependence of the Drell-Yan cross section per nucleon at small x_2 observed in E866. Thus, EKS98 was used to correct the E866 data for nuclear shadowing.

The small residual nuclear dependence observed in E866 as a function of x_1 was then used to set upper limits on the incident-parton energy loss in each of the three models above. The fits are shown in Fig. 5. E866 found that the fractional energy loss of the incident quarks is less than 0.14%/fm ($1\,\sigma$), when using the model of Gavin and Milana. The incident quarks lose energy at a constant rate of less than 0.44 GeV/fm, when using the model of Brodsky and Hoyer, and the observed energy loss of the incident quarks within the model of Baier *et al.* is $\Delta E < 0.046$ GeV/fm^2 $\times$ L^2, where L is the quark propagation length through the nucleus. These upper limits on the energy loss are tighter than previous direct constraints and are consistent with the preliminary results from RHIC.

An alternative approach has been adopted to determine incident-parton energy loss in a recent reanalysis [38] of the E772 Drell-Yan nuclear dependence study. This work fits the E772 Drell-Yan nuclear dependence with the combination of a "first-principles" calculation of the nuclear shadowing in Drell-Yan scattering, based on the coherence length of $q \leftrightarrow q\gamma^*$ fluctuations as observed in the target nucleus rest frame, and a colored-string model for parton energy loss. It concludes that the average incident-parton energy loss is $2.32 \pm 0.52 \pm 0.5$ GeV/fm, in clear contradiction to the less than 0.44 GeV/fm result from the most similar E866 analysis. Approximately half of this difference originates from different treatments of the path length through the nuclear matter. The E866 analysis took the path length to be the average propagation distance within the nucleus prior to the hard scatter that produces the Drell-Yan pair, whereas the recent E772 reanalysis takes the path length to be the average propagation distance from the first inelastic scattering, when the colored string is formed, until the hard scatter occurs. The rest of the difference can be traced ultimately to the two different treatments of nuclear shadowing. In particular, the "first-principles" calculation predicts much less shadowing than the EKS98 parametrization and, thus, requires considerably more energy loss to fit the experimental data.

At present, it is unclear which approach to evaluate the shadowing is more appropriate for the existing experiments. The coherence-length approach is based on well-defined QCD principles and is particularly attractive at very small x_2. Similar calculations of shadowing in deep-inelastic scattering do a very good job of describing the data at small x. However, for $x > 0.06$, the coherence-length calculations fail to reproduce the nuclear dependence observed in deep-inelastic scattering. This is notable because most of the E772 Drell-Yan events have $x_2 > 0.06$. Furthermore, the large apparent energy loss found using the coherence-length approach appears to be inconsistent with the preliminary results from RHIC. In contrast to the "first-principles" shadowing calculations, EKS98 is based primarily on *ad hoc* parametrizations of the nuclear dependence seen in deep-inelastic scattering that have only limited theoretical motivation, but which nonetheless describe its observed x and Q^2 dependence quite well. However, EKS98 also included E772 Drell-Yan data at $x_2 > 0.08$ in its fit. While most of the E866 statistics had x_2 well below this, there is a concern that some incident-quark energy loss may have been folded into the EKS98 shadowing fit inadvertently, thus obscuring the effect of energy loss during the E866 analysis.

The best way to resolve this question is to perform a second Drell-Yan nuclear dependence study at a substantially lower beam energy. This amplifies the expected effect substantially, as seen in the $1/s$ dependence of Eqs. 12 and 13. Main Injector energies are ideal for such a study. One would like to observe the nuclear dependence of Drell-Yan scattering as a function of x_1 for moderate values of x_2, where all models predict the cross section per nucleon should vary from nucleus to nucleus by no more than a few percent. We propose to observe the x_1 dependence for those events that have $0.1 < x_2 < 0.2$. This x_2 region is comfortably above the traditional shadowing domain and below the momenta where the EMC effect and/or Fermi motion may modify the target antiquark densities. It was also investigated with moderate statistics by E772, providing a basis for comparison of events at comparable x_2 but quite different x_1. Figure 6 shows the statistical accuracy that we will obtain for the Drell-Yan nuclear dependence as a function of x_1 during P906. We expect the systematic uncertainty in the cross section ratios to be approximately 1%. The cross section ratios in the figure have arbitrarily been set equal to 1. Only events which will

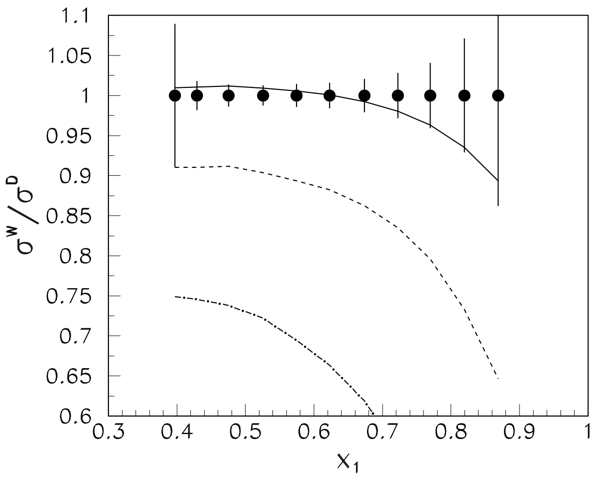

Figure 6: Expected statistical accuracy of P906 for the ratio of the Drell-Yan cross sections per nucleon for W/D vs. x_1. Only events with $0.1 < x_2 < 0.2$ and effective mass above 4.2 GeV/c^2 have been considered. The systematic uncertainty in the cross section ratios is expected to be approximately 1%. The cross section ratios have arbitrarily been plotted at 1. The solid curve shows the expected cross section ratio for a fractional energy loss of 0.14%/fm (Eq. 11). The dashed curve shows the expected cross section ratio for a constant energy loss of 0.44 GeV/fm (Eq. 12), based on the procedures used to estimate path lengths in the E866 analysis. The dot-dashed curve shows the expected cross section ratio for a constant energy loss of 2.32 GeV/fm, based on the procedures used to estimate path lengths in the reanalysis of E772.

satisfy the trigger and pass the target and dump cuts that have $0.1 < x_2 < 0.2$ and effective mass above 4.2 GeV have been included. Comparable statistics will be obtained for the cross section ratios for the other two nuclear targets. To demonstrate the sensitivity of this measurement to incident-parton energy loss, we have also calculated the x_1 dependence that we would expect for an energy loss equal to the upper limits found by E866 for models (11) and (12) above and for an energy loss equal to the result found from the "first-principles" reanalysis of the E772 experiment. The expected x_1 dependence of the cross section ratio per nucleon for W/D in model (13) is similar to that for model (12), but the two models will be distinguished by their different predicted A dependences. Overall, P906 will be a factor of 5 to 10 more sensitive to incident-parton energy loss than E772 or E866. The ultimate sensitivity will be limited by our ability to separate incident-parton energy loss effects from nuclear modifications of the target antiquark distributions, which will be determined largely by the results of the target antiquark studies that are also planned for P906.

2.3 Antiquark Distributions of Nuclei

In the context of nuclear convolution models, virtual pion contributions to nuclear structure functions were expected to lead to sizable increases in sea distributions of the nuclei compared with deuterium. This expectation was convincingly shattered by the E772 Drell-Yan measurements [32], as shown in Fig. 7, which found little nuclear dependence except in the

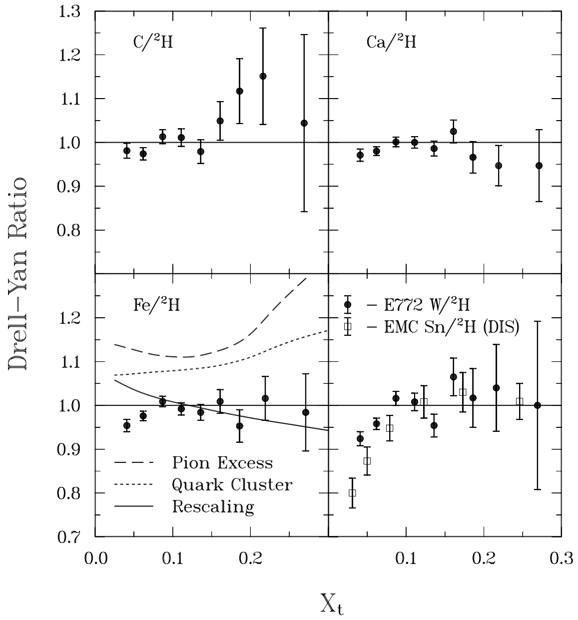

Figure 7: E772 measurements of the ratio of Drell-Yan cross sections on nuclear targets to deuterium [32].

shadowing region. The non-observation of evidence for nuclear pions or a pion excess calls into question the most widely believed traditional meson-exchange model [39] of the nucleus. The absence of the anti-quark excess associated with pion exchange is a fundamental problem for nuclear physics. The expected enhancement to the sea is illustrated in Fig. 8, which shows the expected ratio of $\bar{u}$ in iron to $\bar{u}$ in deuterium which is based on the nuclear convolution model calculations by Coester [40]. This should be directly comparable to the iron to deuterium ratio measured by E772. More recent calculations, made in light of the E772 data, predict a smaller nuclear dependence, consistent with the statistical uncertainties of E772 [41, 42, 43]. Unfortunately, for $x > 0.2$, the E772 statistical uncertainties allow considerable freedom for these models. At $x \approx 0.3$ these models have nuclear effects of the order 5 to 15% in the Drell-Yan ratio.

High precision Drell-Yan measurements at x larger than E772 could access would provide extremely valuable new information on the nuclear dependence of parton distributions. Drell-Yan data on nuclear targets will allow direct comparisons with antiquark distributions obtained from neutrino data on nuclear targets to be made. For the first time, we would have the sensitivity to see the reduction in the nuclear sea distributions predicted in the Q^2 rescaling models [41] and differentiate this from other models which predict an enhancement in the Drell-Yan ratio. In addition, it will constrain possible nuclear effects in the $\bar{d}_p/\bar{u}_p$ measurement. A large rise in the nuclear ratio would provide an important alert that nuclear effects may be important in the deuterium to hydrogen ratio. The expected statistical precision of the proposed measurement is shown in Fig. 9, compared with the existing Drell-Yan and deep inelastic scattering results on the ratios of calcium to deuterium.

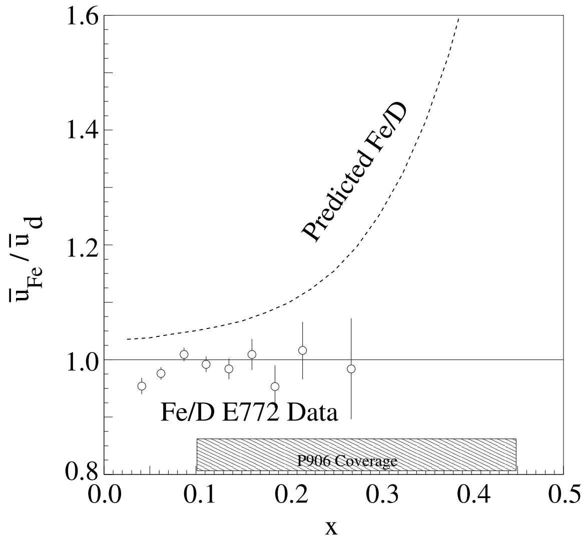

Figure 8: Ratio of $\bar{u}$ iron to $\bar{u}$ in deuterium as calculated by Coester [40] including both nuclear motion and pion contributions, which should be directly comparable to the E772 data [32]. The shaded box shows the x coverage of this proposal.

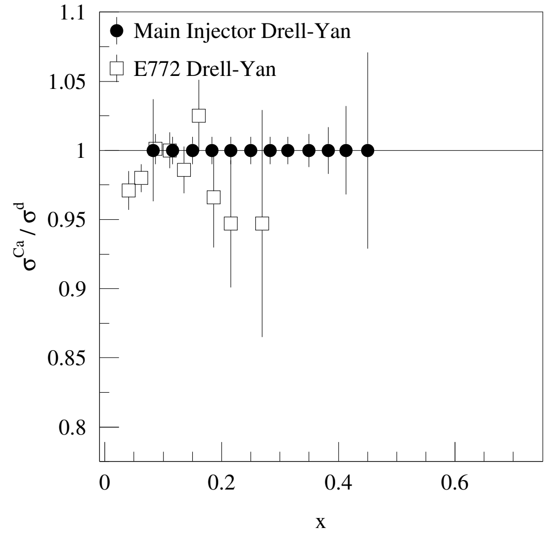

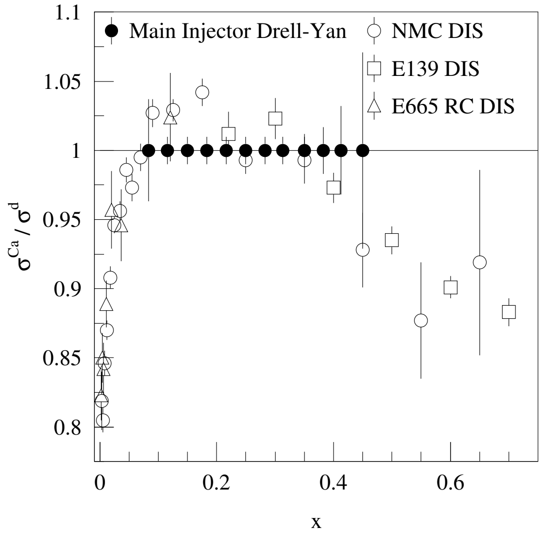

Figure 9: FNAL E772 Drell-Yan results (left) and a compilation of deep inelastic scattering (right) results on the ratio of cross sections of calcium to deuterium, compared with the statistical uncertainties of the proposed measurement (which are arbitrarily plotted at 1.0). The systematic error is expected to be less than 1%.

2.4 Possible Future Measurements

This proposal focuses on measurements of Drell-Yan $\mu^+\mu^-$ production with the primary proton beam. A number of other interesting measurements could be made with this spectrometer. We have previously submitted a letter of intent for Drell-Yan measurements with polarized protons on a polarized proton target to determine the spin structure of the sea distributions. When a polarized proton beam becomes available from the Main Injector, the present apparatus would be immediately suitable for that experiment. Even with an unpolarized beam there appear to be interesting correlations one can measure with Drell-Yan on a polarized proton target [44]. Intense secondary meson beams would open up new possibilities such as a more accurate determination of the charged kaon valence parton distributions or measurements of the ratio of d/u distributions of the proton as $x \to 1$.

While the production of the heavy $\bar{q}q$ pair from gluon-gluon fusion or quark-antiquark annihilations can be perturbatively calculated, the long-distance process involving the formation of the bound states is presently not amenable to calculation. Measurement of the polarization of produced quarkonia states can be used to understand the long-distance process. Fermilab E866/NuSea had made detailed measurement of J/ψ and Υ polarization [45]. A very interesting, complimentary measurement would be the polarization of the $\psi\prime$. A reconfiguration of the absorber wall (described in section 3.2) would allow for this study. In addition, with the reconfigured absorber, a study of the nuclear dependence of J/ψ production at lower beam energy could be done. The nuclear dependence of J/ψ and ψ' production was studied at 800 GeV/c in E866 [46] and at 200 GeV in NA3 [47]. The results appear to scale with x_F, but this could be examined with nuch higher statistical precision in the proposed detector than was achieved by NA3.

3 Experimental Apparatus

The experimental apparatus leans heavily on the E605, E772, E789 and E866 experience for the best technique to handle high luminosities in fixed target Drell-Yan experiments. The key features of the apparatus are:

- Relatively short (<15% interaction length, L_I) targets to minimize secondary reactions in the target.
- Two independent magnetic field volumes, one to focus the high transverse momentum muons and defocus low transverse momentum muons and one to measure the muon momenta.
- A 15 L_I hadron absorber to remove high transverse momentum hadrons.
- A 30 L_I beam dump at the entrance of the first magnet.
- Zinc and concrete walls for muon identification at the rear of the apparatus.
- Maximum use of existing equipment consistent with the physics goals.

As will be discussed below, the apparatus can be almost completely constructed by reusing or refabricating existing equipment. Only the first magnet requires a significant construction effort.

While the lower beam energy is a great advantage in terms of cross section and background rates and statistics, it has two disadvantages relative to 800 GeV experiments.

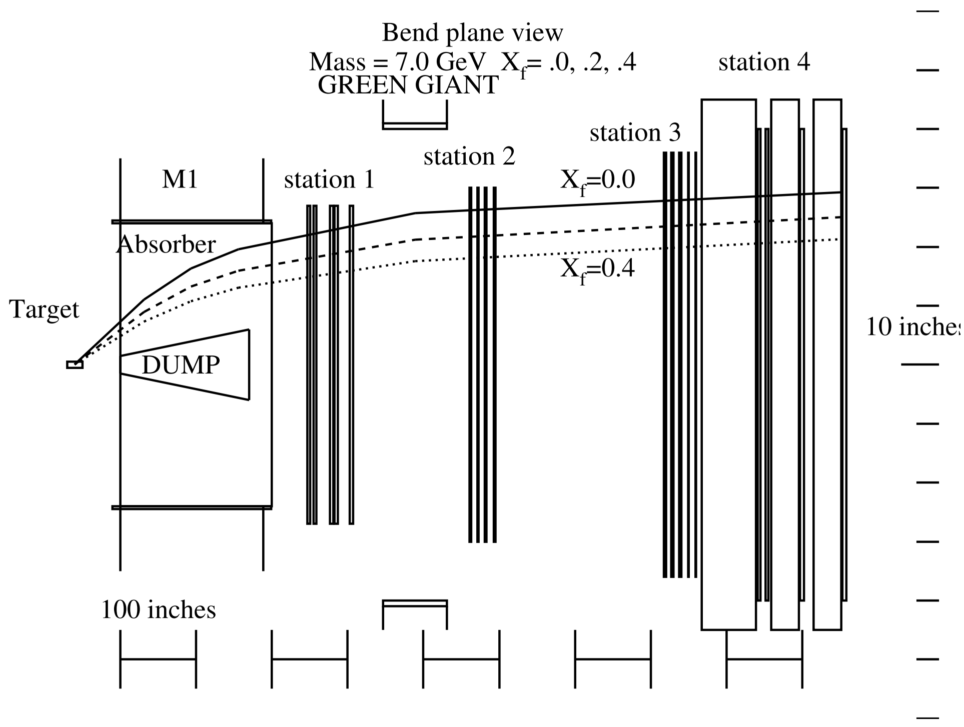

Figure 10: Bend plane view of the trajectories of one of the two muons resulting from the muon decay of a 7 GeV virtual photon (which has x_F of 0.0, 0.2 or 0.4) in an 8 T-m spectrometer.

- The corresponding lower particle energies lead to increased probabilities for muonic decay of the produced hadrons. This is partially compensated by reducing the target-to-hadron-absorber distance to 1.3-1.8 m.
- The lower energy muons multiple scatter more easily in the hadron absorber.

We wish to optimize the design for events with large x_2 and $x_F \approx 0.2$. For scale, the muons generated by a 7 GeV virtual photon with $x_F = 0.2$ which decay perpendicular to the direction of motion (in the virtual photon rest frame) will in the laboratory have momenta of 33 GeV, an opening angle of 210 mr and transverse momenta of 3.5 GeV.

A sketch of the apparatus showing trajectories for muons from 90° decays at $0 < x_F < 0.4$ is shown in Fig. 10 (bend plane view) for a 7 GeV mass virtual photon. Figure 11 illustrates the non-bend plane view. The coordinate system has Z along the beam axis with z=0 at the upstream face of the first magnet. X is horizontal, (beam West) and Y is vertical, increasing upward, for a right handed coordinate system.

3.1 Beam and Targets

The requirements for the beam are 10^{12} protons per pulse with a maximum beam spot size of 5 mm vertical by 10 mm horizontal and maximum divergence of 2 mr in each direction. The primary beam will stop in a 170" long trapezoidal copper beam dump starting with a 3" vertical height at z=0 extending to a 12" vertical height at z=170". Since the dump

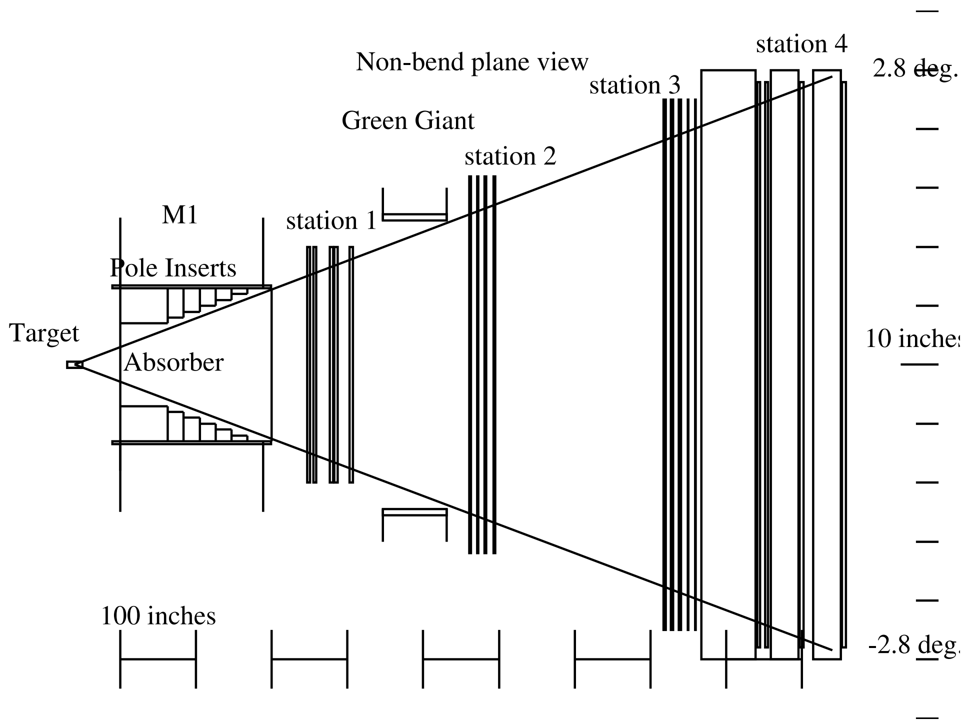

Figure 11: Non-bend plane view in an 8 T-m spectrometer. Only muons which pass around the beam dump in the bend plane contribute to the acceptance and so the beam dump is not shown.

will absorb an average of 6400 watts of beam power, we anticipate it would be water cooled with a closed loop recirculation system like the E866 dump.

The experiment would use 20" long liquid hydrogen and deuterium targets, three nuclear targets of approximately 10 gm/cm^2 thickness and a dummy liquid target cell. The targets would be remotely interchanged roughly every 30 minutes. The rapid Main Injector spill cycle will require blocking the beam for on the order of 30 sec to allow for target motion. The exact choice of nuclear targets has not been made but they are likely to be carbon, calcium or iron and tungsten. An advantage of iron would be a more direct comparison with the CCFR data. Tungsten would extend the nuclear dependence studies to a heavy nucleus, especially for the energy loss studies.

Since the end of the target is located only 1.3 m from the beam dump. We anticipate installing a remotely movable Pb curtain between the target and the dump to reduce the radiation impact on target service operations.

3.2 Magnets

The purpose of the first magnet of the spectrometer is to contain the high transverse momentum muons and to bend low momentum muons out of the experimental acceptance. The optimal performance would be obtained with a approximately 2.5 GeV p_T kick ($\approx$ 8 T-m) large aperture 48" (y) by 26" (x) magnet. Reasonable Drell-Yan acceptance may be retained, provided the aperture of the downstream spectrometer is large enough, for lower field integrals but the singles rates dramatically increase to an unacceptable level. Even

Table 1: The characteristics of the proposed M1 and the Jolly Green Giant magnet. The M1 horizontal aperture is without the pole inserts.

Property	M1	Jolly Green Giant
Length	189 in	84 in
Width	95 in	135 in
Height	198 in	190 in
Vertical Aperture	48 in	96 in
Horizontal Aperture	26 in	49.14 in
Field Integral	8.14 T-m	1.65 T-m
Ampere-Turns	670230	101000
Current	2394 Amp	980 Amp
Power	0.58 MWatt	0.89 MWatt
Inlet Water Temperature	38°C	35°C
Temperature Rise	25°C	22°C
Water Flow	88 gal/min	152 gal/min
Weight:		
Pole Inserts	9.5 t	
Coils	19 t	
Return Yoke	420 t	
Total	450 t	220 t

with the present design we must be prepared for 100 MHz instantaneous rates in the first set of wire chambers.

An 189" long 8 T-m large aperture magnet can be constructed using 33% of the iron from SM12 in Meson East with new coils, following the same general principles as SM3. The characteristics of this magnet are given in table 1. Iron inserts will provide a tapered horizontal aperture of 98 mr opening angle tailored to the aperture of the second magnet. By using existing iron pieces for the return yoke, there should be minimal need to machine the radioactive iron. With such a magnet, there appear to be no experimental barriers to completing the measurement proposed here. The aperture around the beam dump is filled with a graded hadron absorber consisting of 80" of graphite, followed by 40" of copper then 40" of graphite and 40" of Borated Polyethylene.

The muons will lose approximately 3.5 GeV in energy passing through the absorber and multiple scatter by an average angle of $170/p_\mu$ mr. This level of multiple scattering will still permit acceptable virtual photon mass resolution (approximately 240 MeV) and acceptable vertex resolution to separate target and beam dump events for muon energies greater than 15 GeV. Due to the long target length relative to the target-to-absorber distance, the target position provides minimal additional track constraints for the mass measurement.

The second magnet must provide the accurate momentum determination and have a large acceptance. The existing SM3 magnet would be ideal, but is being moved to C0. The most suitable available FNAL magnet appears to be the Jolly Green Giant (JGG) which is currently in Lab G. At present, the JGG has a turn-to-turn short in one of its coils. We would need to have the short repaired to improve the p_T kick to 0.5 GeV (estimates of the

Table 2: Wire Chamber Specifications and Singles Rates

Station	Type	x size (cm)	y size (cm)	wire spacing (mm)	wire orientations	Number of Channels	Singles Rates (MHz)
1	MWPC	101.6	137.2	2.0	Y,U,V,Y,Y',U',V'	7000	40
2	DC	137.7	149.9	10.2	Y,Y',U,U',V,V'	1000	10
3	DC	203.0	162.4	20.3	Y,Y',U,U',V,V'	700	2
4	Prop. Tubes	254.0	211.0	10.0	Y, Y', X, X'	900	2

cost of the repair are available). The characteristics of the Jolly Green Giant are also given in table 1.

We also expect that for radiation protection purposes, the spectrometer, like the Meson-East spectrometer, will need to be vertically bending. If so the JGG would require modification to accommodate this since it is presently configured as a horizontal bending (vertical field) magnet.

If the Jolly Green Giant or another comparable magnet is not available, a suitable replacement could be constructed following the same techniques and using another 8 pieces of the SM12 return yoke. The coil cost would be roughly half of the cost of the new coil for M1. This would effectively be a copy of SM3 but with only half the field integral.

The absorber configuration was optimized based on GEANT simulations. The 40" of copper helps to eliminate particles which escape from the dump. The instantaneous single rates at each of the detector stations are given in table 2 The dominant single contribution is muons from the decays of hadrons in the dump.

3.3 Tracking Chambers

The high instantaneous rates at station 1 lead us to plan for rates up to 100 MHz. We propose to use Multi-Wire-Proportional-Chambers with a 2 mm wire spacing. The first three planes would be MWPC's used in E605 with existing electronics. The stereo angles of the U and V wires are ± 14 degrees. The following four planes would use two existing E871 MWPC's, each covering half the x acceptance arranged with a 4" horizontal gap at $x = 0$. The frames of the two chambers would overlap in this gap. While multiple scattering in the frames does not significantly deteriorate the resolution, this $x = 0$ stripe avoids the highest count rate areas (at the maximum y). The stereo angle of these planes is ± 26 degrees. Existing E871 preamplifier-discriminator-readout would be used. Each of these wire chambers has 3 rf bucket hit resolution and would run with a fast gas (CF4/isobutane, 80:20). The readout would consist of 7000 channels of coincidence registers. All the electronics and readout currently exist (E871 has 20000 wire chamber channels).

Stations 2 and 3 would use the existing E605/E772/E866 drift chamber stations 2 and 3. They are capable of 250 μm resolution with Ar/Ethane (50:50) gas. The stereo angle is ± 14 degrees. Existing preamplifiers and discriminators would be adequate. A 1700 channel multi-hit TDC system is required for good efficiency and rate capabilities. A more than sufficient number of LRS 3377 modules are expected to be available from PREP [48].

Station 4 would be constructed of limited streamer tubes with a 1 cm pitch operated in proportional mode using existing amplifiers and discriminators from E866. Readout would be identical to the MWPC's and add 900 channels to the electronics and coincidence register total.

We have studied the rate dependence of the pattern recognition efficiency in Monte Carlo simulations to ensure that this choice of chamber configuration is acceptable. With 2.5 times the rates given in table 2, we find only a 4% decrease in efficiency, on the same scale with the level of rate dependent effects we were able to deal with in E866.

3.4 Scintillator Hodoscopes

Scintillator hodoscope planes will provide the hit information for the hardware trigger system, just as they have in E866. There will be a total of eight planes, four to measure track y (bend plane) locations and four to measure track x locations. There will be a y hodoscope plane associated with each of the four detector stations—referred to as Y1, Y2, Y3, and Y4. They will contain 32 channels apiece, separated into 16 channels on the right side of the spectrometer ($x < 0$) and 16 channels on the left side ($x > 0$). There will be x hodoscope planes associated with detector stations 1 and 2, plus two additional planes as part of station 4 – referred to as X1, X2, X4A, and X4B. They will contain 32 channels apiece, separated into 16 channels for the lower half of the spectrometer ($y < 0$) and 16 channels for the upper half ($y > 0$). This segmentation will provide a logical division of each hodoscope plane into quadrants, allowing the trigger system to place tighter geometric constraints on the tracks than was done during E866.

All of the scintillators within a given y hodoscope plane will be the same size. The individual scintillators within hodoscope planes X4A and X4B will all be the same angular size. In contrast, the four X1 and four X2 scintillators closest to $x = 0$ will subtend half the angular range, and the scintillators furthest from $x = 0$ will subtend 1.5 times the angular range of the X4A and X4B scintillators and the remaining X1 and X2 scintillators. This segmentation minimizes the number of hodoscope channels in stations 1 and 2 that may be in coincidence with given channels in X4A and X4B, after accounting for the multiple scattering of the muons through the various absorbers in the spectrometer.

While many of the hodoscopes could be fabricated primarily by recutting and polishing the existing E866 scintillators to the sizes required for the new spectrometer, we believe it is safer, given their age, to plan on constructing new scintillators and light guides for this experiment. We propose to reuse the phototubes and bases from the existing E866 spectrometer and purchase 60 new phototubes and bases for the additional channels. The existing E866 high voltage distribution systems will suffice to power the eight hodoscope planes.

For E866, the anode signals from each phototube were sent to LeCroy 4416 leading-edge discriminators. The discriminator outputs were reshaped by custom synchronizer/stretcher modules to provide clean, single RF bucket time resolution for all hodoscope planes except station 4, which had slightly worse than single bucket resolution. The higher background rates anticipated at the Main Injector due to the increased beam current make it very important to achieve clean, single RF bucket time resolution for all hodoscope planes. Given past experience, this should be straightforward with the existing discriminators for the hodoscopes in stations 1 and 2, and for the X4A and X4B planes. The longest scintillators in the spectrometer, those for Y4, will be only 7" shorter than the station 4 scintillators during E866 and we propose to use phototubes on each end of these scintillators and 32 channels of mean timers to provide single bucket resolution. We already have enough synchronizer/stretcher modules in hand to instrument the entire new spectrometer.

3.5 Muon Identification

Final muon identification is provided with an absorber wall, 81 cm of concrete followed by 92 cm of zinc and 10 cm of Pb, followed by 2 planes of streamer tubes and the X4A scintillators, then 92 cm of concrete followed by the Y4 and X4B scintillators and finally 92 cm of concrete followed by 2 planes of streamer tubes. The present E866 muon identification walls provide enough material for the smaller P906 wall [25].

3.6 Trigger

The hardware trigger system will examine the scintillator hodoscope hits to identify patterns characteristic of high mass muon pairs produced in the target. It will be conceptually similar to the system that was developed for E866 [49]. However, it will be enhanced substantially compared with the previous system, primarily to improve its ability to reject random coincidences that appear to form a candidate high p_T muon track. Such random coincidences represented over half of the apparent muon tracks observed during the E866 intermediate mass $\bar{d}/\bar{u}$ running, and the background rates in the spectrometer due to soft muons are expected to be even higher at the Main Injector. The trigger modifications will also permit us to implement two-dimensional masking of wire chamber hits during event analysis, based on the active hodoscope roads, which will reduce the combinatorics in the wire chamber track finding. Notably, this will minimize the frequency of hit-bank and track-bank overflows, one of the sources of rate-dependent reconstruction inefficiency that we encountered during E866. Finally, the trigger modifications will permit us to replace a number of custom CAMAC modules from the E866 trigger system that are now nearly 20 years old with new, more reliable and flexible units.

Electronically, the hardware trigger will consist of a single decision stage, implemented as a three-step parallel pipeline. In the first step, the outputs from the hodoscope synchronizer/stretcher modules will be routed to a set of LeCroy 2367 Logic Modules[2]. Eight modules will be dedicated to identifying four-fold Y1-Y2-Y3-Y4 coincidences characteristic of high p_T single muons produced in the target. Each time they observe a candidate track, they will output a bit indicating its charge, the side of the spectrometer (left or right) where it is located, the quadrant the track passed through at Y1, and the actual y location of the track at Y4. In general, Y1-Y2-Y4 triple coincidences would suffice since the spectrometer analyzing magnet is located between stations 1 and 2, and that is in fact how candidate tracks were identified during E866. Adding the extra constraint that the appropriate channel of Y3 must have a hit will help reject apparent tracks that actually consist of a random coincidence between hits in stations 1 and 2 due to one muon and a hit in station 4 due to another.

The $\bar{d}/\bar{u}$ measurement will only be interested in a limited number of potential track roads through the spectrometer. However, the eight LeCroy 2367 modules required to identify all of those tracks contain enough additional internal logic and I/O capability to cover the entire phase space of four-fold Y1-Y2-Y3-Y4 coincidences associated with real

[2]Note that if LeCroy 2367 Modules are no longer available, a custom fabricated electronics solution can easily be found.

tracks originating from either the target or the beam dump. This will provide maximal flexibility when designing triggers for study purposes or ancillary measurements.

Four additional LeCroy 2367 modules will be dedicated to identifying candidate tracks originating from the target that include coincidences among at least three of the four planes X1-X2-X4A-X4B. Each time they observe a candidate track, they will output a bit indicating the side of the spectrometer where it is located, the quadrant the track passed through at X1 and X2, and the actual x location of the track at X4A and X4B. This represents a significant upgrading of the tracking capability of the hardware trigger in the x direction, compared with E866, and will permit us to provide full two-dimensional constraints on the tracks. It will also make continuous monitoring of the efficiency of the y hodoscopes practical. This may prove to be important because our ability to average over long-term variations in the spectrometer efficiency between targets will be reduced at the Main Injector, since we will be unable to change amongst the various targets as frequently as we did during E866. In contrast, for E866 special hodoscope efficiency studies were run every few weeks. They consisted of a series of runs utilizing a special trigger configuration, sequentially turning off the high voltage on sets of x hodoscopes near the center of the spectrometer.

The second step in the trigger pipeline will combine the x and y tracking results from the first step to identify events with candidate high p_T muons present. This will be done in a pair of LeCroy 2367 modules, one dedicated to tracks on the left side of the spectrometer and one dedicated to tracks on the right side. The candidate muons will be characterized according to their charge, the side of the spectrometer on which they are located, and a rough measure of their p_T. Events will also be tagged that appear to have two muons with opposite charges present on the same side of the spectrometer.

In parallel with the first two steps of the main trigger sequence, OR's of all the scintillators on each side of each plane will be generated and routed to a Track Correlator [49] to generate simple cosmic ray and noise triggers for diagnostic purposes. This procedure was utilized during E866, and the same CAMAC and NIM electronics will be reused at the Main Injector.

The final step in the trigger pipeline will generate the actual triggers, handle the experiment busy logic, and strobe the read-out electronics. This step will either be performed with one additional LeCroy 2367 module or with the Track Correlators and Master Trigger OR that were designed and constructed for the E866 hardware trigger [49]. The primary physics trigger will consist of a coincidence between two candidate $x-y$ tracks of opposite charges, on either the same or opposite sides of the spectrometer. If we find that the background trigger rate due to low mass muon pairs is higher than desirable, we will combine the rough measures of the p_T for the two muons from the previous step to provide a crude effective mass cut on the muon pair in hardware. A similar procedure, but with less granularity than we anticipate with the new trigger system, was adopted for several of the data sets taken during E866. For example, it reduced the raw trigger rate during the E866 intermediate mass $\bar{d}/\bar{u}$ data taking by a factor of three, with essentially no reduction in efficiency for the Drell-Yan muon pairs of interest. Two triggers will be used to determine the rate of random coincidences between two muon tracks in the same RF bucket, both of which originate from the target and, thus, are indistinguishable from a real Drell-Yan muon pair. One of these triggers will record events that contain two muons of the same charge when they are located on opposite sides of the spectrometer, while the other will record a prescaled set of single-muon events. E866 has demonstrated that we can obtain an excellent simulation of the random coincidence background by combining muons from single-muon triggers into pairs, then normalizing their number to the observed rate of like-sign coincidences. Two additional triggers will select prescaled samples of events that contain a candidate track in either the x or y direction, but not necessarily both. The events with x tracks will be used to monitor the absolute efficiencies of the y hodoscopes, and the events with y tracks will be used to monitor the absolute efficiencies of the x hodoscopes. The last trigger will provide a luminosity-weighted read-out of all detector elements during random RF buckets, independent of the status of any of the spectrometer hodoscopes. This will be used to provide an unbiased measure of the background occupancy rates throughout the spectrometer, which are very important for estimating rate-dependent reconstruction inefficiencies.

3.7 Monte Carlo of Trigger and Spectrometer Rates

Thorough Monte Carlo simulations have been done to determine both the detector response and resolution, and spectrometer and trigger rates. Two different Monte Carlo codes have been used for these simulations. The primary one is a modified version of the "Fast Monte Carlo" that was originally written to estimate acceptances in E605/E772/E789/E866. It has now been modified to simulate the detector configuration for this proposal, P906. This Monte Carlo simulates muons from Drell-Yan, resonance production (J/ψ, ψ', Υ, $\Upsilon(2S)$, $\Upsilon(3S)$), and π, K and charmed meson decays. It can track single muons or pairs through the entire spectrometer in order to estimate signal and background rates with realistic hardware trigger simulation. It also simulates the traceback of the muon tracks to the target so that realistic tracking cuts may be imposed and the ultimate resolutions of the spectrometer can be estimated. The details of the thrown spectra and assumed cross sections can be found elsewhere [50]. The second code is a GEANT-based Monte Carlo. This code was written to optimize the design of the hadron absorber wall. Unlike the first code, this Monte Carlo only tracks particles as far as Station 1. However, it tracks all particles which arise from proton interactions in the targets and beam dumps, rather than just muons, so it is quite useful for configuring the hadron absorber that will fill the aperture of the large M1 magnet. Both codes have been demonstrated to give a reasonable description of the rates that were observed during E866, and they give consistent results for the flux of muons with momenta above 3 GeV/c that should be present in Station 1 at the Main Injector.

The Fast Monte Carlo code has been verified through a number of further tests. For P906, its prediction of the flux of muons with momenta above 3 GeV/c that should be present at Station 1 is consistent with a full GEANT simulation of the target, beam dump, magnet and absorbers. The simplified muon traceback to the target has been checked by verifying that it reproduces observed resolutions during E866. For example, the predicted and observed J/ψ mass resolutions during the E866 large-x_F nuclear dependence study agree to within 10%.

The Monte Carlo has been used to estimate the trigger rates. The rates of muon pairs from Drell-Yan and resonance production originating in either the target or the dump have been simulated for the equivalent of 10^3 to 10^5 spills at an assumed intensity of 10^{12} protons per spill. The rate due to Drell-Yan pairs off the LH_2 target is 0.55/spill, with approximately half of these passing the tracking and effective mass cuts. The total "real" rate is expected to be approximately 90 events/spill, with approximately 15% of these passing trigger matrix cuts, depending on the target. The vast majority of the events are from J/ψ's produced in the beam dump and do not pass trigger requirements. Of the triggered events, approximately two thirds originate from Drell-Yan pairs produced in the beam dump. The yield of muon pairs from $D\bar{D}$ production is very small. At $\sqrt{s} = 15$ GeV,

Table 3: Expected rate of events which traverse the detector and trigger rates per spill from real and random coincidences with liquid hydrogen and deuterium targets and the copper beam dump. The ratio of deuterium to hydrogen rates reflects the difference in the densities of liquid deuterium and hydrogen. Note that the random coincidences for each target include contributions from the beam dump.

	LH_2		LD_2		Copper Beam Dump	
	Evts.	Trig.	Evts.	Trig.	Evts.	Trig.
Drell-Yan ($m_\gamma > 3\text{GeV/c}^2$)	0.55	0.35	1.47	0.93	17.6	7.8
J/ψ, ψ'	2.53	0.23	6.03	0.56	72.0	3.4
$\bar{D}D$	> 0.01	> 0.01	0.01	> 0.01	0.11	> 0.01
random coincidences		≈ 50		≈ 100		-

there will be very few Υ events ($m_\Upsilon = 9.5$ GeV/c^2) over the life of the experiment. These rates are summarized in table 3.

In addition to the real pairs, there will be a significant number of triggers from random coincidences of two independent muon tracks. When running with the liquid hydrogen target, the primary source of background single muons will be π and K decay-in-flight in the beam dump. When running with the liquid deuterium target, the π and K decay-in-flight background from the target will be slightly larger than that from the dump. The total rate of single muons traversing the detector and passing the trigger will be approximately trigger rate will be approximately 48 kHz with the LH_2 target and 71 kHz with the LD_2 target. In each case, the Monte Carlo predicts that the ratio of positive to negative muons will be approximately 2:1. These rates are shown in table 4. To obtain a conservative estimate of the trigger rate, we have chosen to double the predicted rates of true single muon triggers in order to account for random contributions to the single muon rate and finite duty-factor of the proton beam when estimating the random pair rates. This leads to estimates of 50 random dimuon triggers per spill for the LH_2 target and 100 random triggers per spill for the LD_2 target, counting all random opposite-sign pairs and the random like-sign pairs that have one muon on each side of the spectrometer. These random trigger rates do not include the additional suppression that we will obtain by constraining the apparent mass of the pair in hardware. Experience from E866/NuSea indicated that these random pairs will have a mass spectrum strongly peaked at masses near or below the J/ψ.

We will also take approximately 80 study triggers per spill—including prescaled single muons to study the random background, triggers to monitor the efficiency of the hodoscopes, and triggers to investigate any rate-dependence that may be present in the data analysis. Therefore, overall we expect approximately 200 triggers or less per spill. We will assume a trigger rate of 1 kHz for planning purposes. With full analysis cuts, the real to random rate is expected to be 5 to 1 at all x_2 values, and much better than that at large x_2.

Most of the background triggers are eliminated in the analysis by simple cuts based whether the track points back to the target and the track's proximity to the beam dump. Histograms of these quantities are shown in Figs. 12 and 13, respectively. For the purpose of estimating reconstructed track rates, an accepted track needed to pass within 5.7 cm of the target in y and be at least 5.7 cm in away from $y = 0$ cm at the front face of the

Table 4: Expected single muon rates per spill from decay-in-flight mesons which pass through the detector (μ's) and satisfy trigger matrix tracking requirements (Trks.) from liquid hydrogen and deuterium targets and the copper beam dump.

	LH_2		LD_2		Copper Beam Dump	
	μ's	Trks.	μ's	Trks.	μ's	Trks.
π^+ decay-in-flight	40.6 k	6.1 k	97.7 k	14.6 k	75.9 k	6.5 k
π^- decay-in-flight	17.4 k	4.1 k	41.9 k	9.8 k	38.2 k	10.1 k
K^+ decay-in-flight	31.5 k	6.5 k	75.8 k	15.6 k	69.6 k	10.3 k
K^- decay-in-flight	3.1 k	1.3 k	7.6 k	3.1 k	8.8 k	4.2 k

beam dump. Clearly these restrictions will remove the vast majority of unwanted tracks. In addition, to remove contamination from the ψ and Υ resonance families, the mass of reconstructed muon pair must be between 4.2 GeV/c^2 and 8.8 GeV/c^2.

In addition to trigger and spectrometer rates, the Monte Carlo was also used to estimate the expected resolution of the detector. For simulated Drell-Yan events which pass the trigger and reconstruction cuts, the expected mass resolution is $\sigma_m = 200\mathrm{GeV/c}^2$ and the x_2 resolution is $\sigma_{x_2} = 0.02$. These are shown in Fig. 14.

3.8 Data Acquisition System

In order to achieve the goals put forward in this proposal, the data acquisition system must be able to: (1) digitize and move to tape detector hits from MWPC's, hodoscopes, streamer tubes and drift chambers at trigger rates of up to 1 kHz with very small dead time; (2) include information on the trigger condition in the data stream; (3) provide for on-line monitoring of detector efficiencies and the status of main system components; (4) provide for control of experimental systems such as moving targets and programming trigger modules. All of these capabilities were available in the DAQ system which was used for Fermilab experiment E866. However, several features of the E866 system must be changed to accommodate the MI experiment.

The readout system for E866 used the TRANSPORT interface, which was built by the NEVIS electronics group in 1980, to hoist data from custom built TDC's and coincidence registers to tape. Many problems were encountered with that system during the startup of E866. We also experienced intermittent problems with it during data acquisition. Both the age of the system and the constraints that it imposes on the data stream require that we replace it for the MI experiment. Because they are to operate in a high rate environment, the drift chambers for the MI experiment need to be read out with multi-hit TDC's which precludes using the TDC's from the E866 readout system.

Most of readout requirements for the proposed experiment can be met by the front end system that has been assembled for Fermilab experiment E871. We request that the CR's, FEM's, interface and buffer memory and one VME system used by E871 be moved to this MI project. The E871 system will provide a high speed readout path for the MWPC's, hodoscopes and proportional tubes configured here. We will add multi-hit TDC's, and the appropriate interface connection to the Processor Bus, to read out the drift chambers.

The computer architecture used in E871 is very similar to that planned for this project.

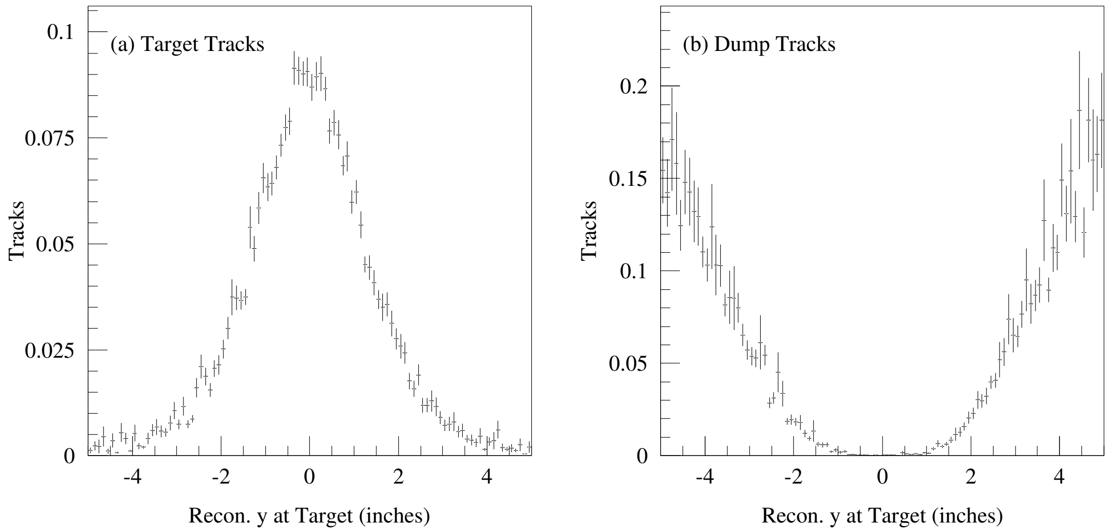

Figure 12: Distance in y of reconstructed track from target center for (a) Drell-Yan and ψ events produced in the target and (b) Drell-Yan and ψ events produced in the dump. To be considered as an event from the target, *both* tracks must reconstruct within 2.25 inches of $y = 0$.

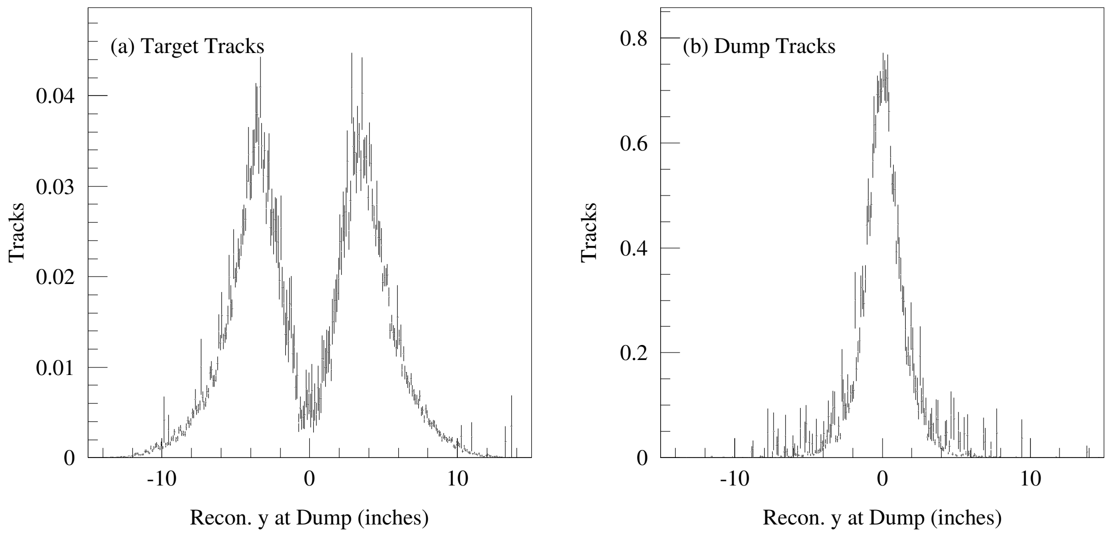

Figure 13: Distance in y of reconstructed track from the beam dump center at the face of the dump for (a) Drell-Yan and ψ events produced in the target and (b) Drell-Yan and ψ events produced in the dump. To be considered as an event from the target, *both* tracks must reconstruct at least 2.25 inches away from $y = 0$ at the dump.

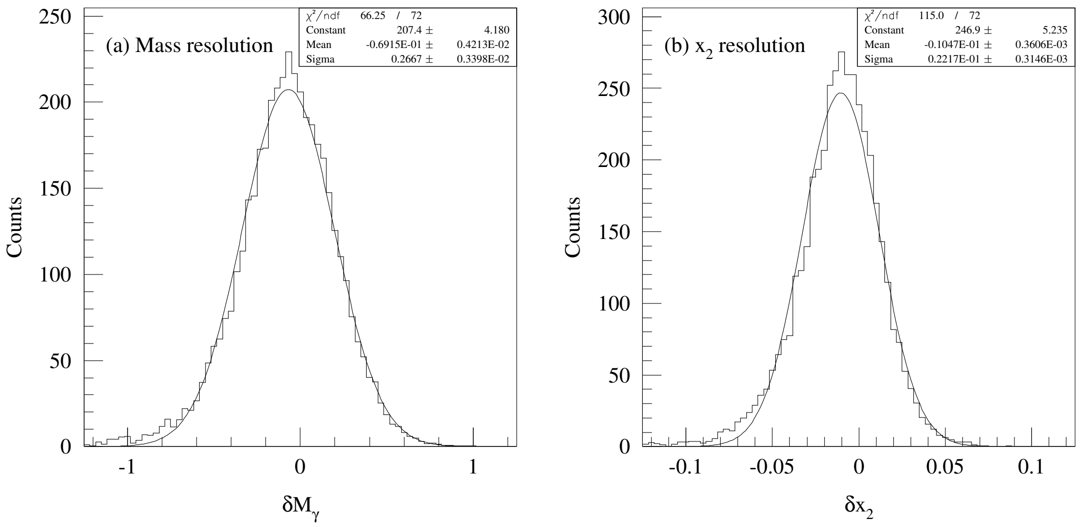

Figure 14: Expected (a) mass and (b) x_2 resolution for accepted Drell-Yan event using the proposed detector.

Our trigger rates, however, will be much lower than those for E871 and event lengths will be comparable so the dead time using their system should be extremely small. As in E871, data will be moved from front end modules to buffer memory and then written out on DLT units. One DLT should suffice to handle the bandwidth since we anticipate average event lengths of less than 1.5 kbytes and trigger rates less than 1 kHz. Event sampling will be done to monitor wire chamber and hodoscope efficiencies using UNIX based workstations or PC's running LINUX.

The DAQ system for this project will follow DART standards and use DART software. This represents another break from the E866 system which did not use DART. The E871 DAQ system uses DART so the front end readout is already compliant with DART standards. With the exception of trigger programming, the remaining system requirements for the MI experiment proposed here are already available in DART software packages.

3.9 Analysis

The analysis of the data accumulated in these measurements should be straightforward, both in offline production and for online monitoring. We expect that the analysis will be similar to that done for E866 and would employ farms of LINUX PC's. An estimate of the scope of the analysis task can be made from the expected trigger rate of 1 kHz (1/3 kHz average), estimated event size of 1.5 kbytes, and a compute time per event of 20 ms/event (on an 180 MHz HP PA8000) based on analysis of data in E866/NuSea. Scaling with floating point performance to a 1 GHz Pentium III (a current "commodity" PC) we estimate that approximately three of these Pentium CPU's can analyze our data as fast as we would take it. In the counting house we generally want to be able to fully analyze about 10 to 20% of the data as it is accumulated and this could be accomplished with only one or two of these PC's. Naturally, since the typical CPU power per dollar increases by perhaps a factor of two per year, by the time this experiment would actually run the hardware available would even more easily address these analysis problems.

The typical taping rate is estimated to be about 0.5 Mbytes/sec (easily within the bandwidth of present Digital Linear Tape (DLT) technology) and would result in about 43 Gbytes of data on tape per day, or about 5 Tbytes for the entire run. To analyze these data as fast as they were taken means the networks that support distribution of the data would need to transport in excess of 0.5 Mbytes/sec, easily within the capability of 100 base-T networks.

Since the planned detector system would be conceptually similar to that used in E866, the analysis algorithms from E866 should be applicable to the new experiment. Therefore we anticipate reusing much of the old code. Since much of the raw data format will probably be new the data unpacking parts of the code would probably be rewritten in C or C++, while other parts that need not change may remain in Fortran. We also would replace the present CMZ code manager with CVS for code maintenance and cpp for conditional compilation. Tools that we have already used for the PHENIX project at RHIC should aid in this conversion. Since our code already runs on the Fermilab UNIX farms using the Fermilab parallel processing environment (CPS), it should be straightforward to preserve that capability. CPS is already ported and being used on LINUX PC farms at Fermilab.

3.10 Yields

Figure 15 shows the results from a Monte Carlo simulation of the expected yields of this spectrometer for a hydrogen target in 90 days at 50% efficiency running. With an 9 month run at 50% total efficiency (66% accelerator, 75% experiment), we would achieve these yields on 5 targets (hydrogen, deuterium and three nuclear targets, relative running time: 35% H, 26% D, 35% nuclear, 4% Dummy liquid cell) and achieve the relative errors on the ratio of the deuterium to hydrogen cross sections for $x_F > -0.1$ shown in Fig. 3. E866 was able to maintain systematic errors on the cross section ratio to better than 1%. We also anticipate being able to achieve 1% systematic errors in the ratio.

With these yields, the statistical precision of the extraction of $\bar{d}/\bar{u}$ is shown in Fig. 16 relative to the expectation with MRST parton distributions.

4 Costs and Schedule

The source and operating responsibility of each component of the apparatus is given in table 5. We are open to having additional collaborators to lead the DAQ and MWPC1 efforts and are talking with several other groups. The expertise for these exists within the collaboration and the equipment in E871 and E866 exists but we have not yet identified the lead groups. Our specific list of requests for Fermilab is separated out in the next section. We have assumed that all the existing equipment from E866 is available for this experiment. We have begun discussions with E871 personnel (Kam-Biu Luk of UC-Berkeley about the wire chambers and wire chamber electronics, Yen-Chu Chen of Inst. of Phys., Academia Sinica about the readout system) about the use of the E871 equipment.

The critical path of the time-line is clearly the construction of the M1 magnet. A preliminary cost estimate is \$1000k for the coil and \$220k for assembly [51]. Following approval of the proposal we will request \$1.3M from DOE-NP for the construction of the magnet coils, inserts and the new hodoscopes[3]. We anticipate the rest of the collaboration contributions coming from continuing research grants. Construction money for the coils

[3]DOE Nuclear Physics is already aware of this request, pending Fermilab approval of this proposal.

Table 5: P906 Apparatus Responsibilities

Component	Subcomponent	Source	Cost (k$)	Responsible Institution
Beam line	Instrumentation			FNAL BD
Target		E866		FNAL PPD
M1	Coils	New	900	ANL
	Inserts	New	100	ANL
	Return Yoke	E866		FNAL PPD
	Assembly	New	220	FNAL PPD
	Power Supplies	E866		FNAL PPD
Jolly Green Giant	Repair Coil			FNAL PPD
	Assemble in Meson			FNAL PPD
	Power Supplies	E866		FNAL PPD
Station 1 MWPC	Chambers	E871/E866		ACU, FNAL
	Electronics	E871/E866		ACU, FNAL
	Readout	E871		ACU, FNAL
Station 1 Hodoscopes		New	20	ACU
Station 2 DC	Chambers	E866		Rutgers
	Electronics	E866		Rutgers
	Readout	New		FNAL PREP
Station 2 Hodoscopes		New	30	ACU
Station 3 DC	Chambers	E866		Rutgers
	Electronics	E866		Rutgers
	Readout	New		FNAL PREP
Station 3 Hodoscopes		New	30	ACU
Station 4 Prop. Tubes	Chambers	New	30	LANL
	Electronics	E866		LANL
	Readout	E871		LANL
Muon ID Wall	Assembly	E866		FNAL PPD
Gas System	Mixing	New		LANL
	Distribution	New		FNAL PPD
Station 4 Hodoscopes		New	80	ACU
Trigger		E866/New	15	TAMU
	LRS2367	New	56	FNAL PREP
DAQ	Hardware	E871		ANL
	Software	E871/New		VALPO,TAMU
Analysis	Software	E866		Lead - LANL

FNAL BD – Beams Division
FNAL PPD – Particle Physics Division
FNAL PREP – Physics Research Equipment Pool

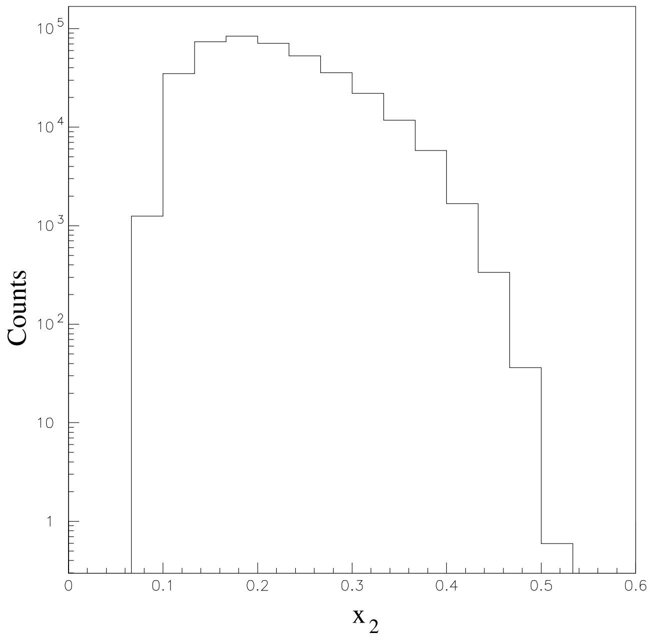

Figure 15: Monte Carlo results for yields from a 90 day 50% efficiency run with 10^{12} protons per pulse on a 20" long liquid hydrogen target with the apparatus shown in Figs. 10 and 11. This represents all accepted events with masses between 4.2 and 8.5 GeV with $x_F > -.1$. The number of counts will be the same on the nuclear targets and 70% greater on deuterium.

could not become available before FY2003. We estimate a one year coil construction and four month assembly process. This will allow us to easily have the experiment on the floor and ready by FY2006, consistent with the current ideas for the start of the Main Injector fixed target program.

4.1 Requests for Fermilab

We specifically request Fermilab to provide the following items:

- Repair coil of Jolly Green Giant magnet.
- Install Jolly Green Giant magnet in Meson as a vertical bending magnet.
- Assemble M1 magnet in Meson Area with the coil provided by ANL and return yoke from SM12.
- Provide beam dump with closed loop water recirculating cooling system.
- Provide magnet power supplies.
- Provide utilities (power and cooling water) for magnets and power supplies.
- Move and install muon ID absorber walls.
- Provide beam line instrumentation

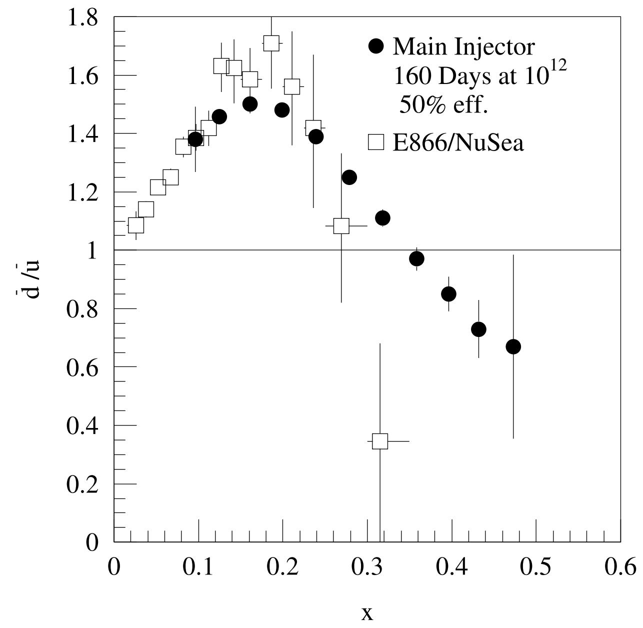

Figure 16: Projected results for the extraction of $\bar{d}/\bar{u}$ from a 160 day 50% efficiency run with 10^{12} protons per pulse on a 50 cm long liquid hydrogen and deuterium targets with the apparatus shown in Figs. 10 and 11 based on the MRST [4] distribution of $\bar{d}/\bar{u}$. Also shown are the E866/NuSea results.

- Provide liquid hydrogen and deuterium targets and drive mechanism to interchange liquid and solid targets remotely.
- Provide prep electronics. Essentially E866 Prep electronics plus 1700 channels of multi-hit TDC (LRS3377), 16 LRS2367 units and 32 channels of mean-timers.
- Provide chamber gas distribution system plumbing.
- Provide flammable gas safety system.
- Provide Rigging for Installation.
- Provide use of Lab 6 facilities for scintillator and light guide fabrication.
- Provide counting house and electronics areas with appropriate utilities installed.
- Provide two analysis workstations for counting house.
- Provide suitable storage for E866 and E871 equipment being reused in this experiment.

5 Collaboration

The core of the collaboration, Abilene Christian University, Argonne National Laboratory, Fermilab, Los Alamos National Laboratory, Texas A&M University and Valparaiso University has recently successfully completed the E866 Drell-Yan experiment at Fermilab. These groups encompass the key technologies needed for the new measurements. The Rutgers group has experience in high rate drift chamber systems. Several other groups have expressed interest in the experiment and we expect little problem identifying sufficient people to construct, operate and analyze the experiment in a timely fashion following a favorable response from Fermilab.

6 Summary

We propose using the 120 GeV primary proton beam from the Main Injector to measure Drell-Yan yields for hydrogen, deuterium and three nuclear targets. These measurements will provide precise new information on:

- the ratio $\bar{d}/\bar{u}$ and the difference $\bar{d} - \bar{u}$ distributions of the proton over the x range of 0.2-0.45 and new insight into the non-perturbative origin of the parton distributions (3.4×10^{18} incident protons),
- the sum $\bar{d} + \bar{u}$ through measurements of the absolute Drell-Yan cross sections,
- the energy loss of colored partons traveling through cold nuclear matter (1.8×10^{18} incident protons), and
- the nuclear dependence of the antiquark distributions over a similar x range.

These measurements should also help resolve nuclear ambiguities inherent in obtaining nucleon antiquark distributions from neutrino data on nuclear targets. The total request for beam with 9 months of running at 10^{12} protons per pulse and 66% accelerator efficiency is 5.2×10^{18} protons.

References

[1] H. L. Lai *et al.*, Phys. Rev. D **55**, 1280 (1997).

[2] H. L. Lai *et al.*, Eur. Phys. J. D **12**, 375 (2000).

[3] A. D. Martin, R. G. Roberts and W. J. Stirling, Phys. Lett. B **419**, 1280 (1997).

[4] A. D. Martin, R. G. Roberts, W. J. Sterling and R. S. Thorne, Eur. Phys. J. **C4**, 463 (1998).

[5] M. Glück, E. Reya, and A. Vogt, Eur. Phys. J. **C5**, 461 (1998).

[6] P. Amaudruz *et al.*, Phys. Rev. Lett. **66**, 2712 (1991); M. Arneodo *et al.*, Phys. Rev. D **55**, R1 (1994).

[7] A. Baldit *et al.*, Phys. Lett. B **332**, 244 (1994).

[8] FNAL E866/NuSea Collaboration, E. A. Hawker *et al.*, Phys. Rev. Lett, **80** 3715 (1998).

[9] FNAL E866/NuSea Collaboration, J.-C. Peng *et al.*, Phys. Rev. D **58**, 092004 (1998).

[10] FNAL E866/NuSea Collaboration, R. S. Towell, submitted to Phys. Rev. D, hep-ex/0103030.

[11] D. F. Geesaman, K. Saito and A. W. Thomas, Ann. Rev. Nucl. Part. Sci **45**, 337 (1995).

[12] A. D. Martin, W. J. Stirling and R. G. Roberts, Phys. Lett. B **252**, 653 (1990).

[13] R. D. Field and R. P. Feynman, Phys. Rev. D **15**, 2590 (1977).

[14] D. A. Ross and C. T. Sachrajda, Nucl. Phys. B **149**, 497 (1979).

[15] F. M. Steffens and A. W. Thomas, Phys. Rev. C **55**, 900 (1997).

[16] W. Melnitchouk, J. Speth, and A.W. Thomas, Phys. Rev. D **59**, 014033 (1999).

[17] P. Geiger and N. Isgur, Phys. Rev. D **55**, 299 (1997).

[18] S. Kumano, Phys. Rev. D **43**, 3067 (1991); **43**, 59 (1991); S. Kumano and J. T. Londergan, Phys. Rev. D **44**, 717, (1991).

[19] A. Szczurek *et al.*, Nucl. Phys. A **596**, 397 (1996).

[20] P.V. Pobylitsa, M.V. Polyakov, K. Goeke, T. Watabe, and C. Weiss, Phys. Rev. D **59**, 034024 (1999).

[21] G. t'Hooft, Phys. Rev. D **14**, 3432 (1976).

[22] A. E. Dorokhov and N. I. Kochelev, Phys. Lett. B **304**, 157 (1993); Phys. Lett. B **259**, 335 (1991).

[23] CDF collaboration, T. Affolder *et al.*, submitted to Phys. Rev. **D**, hep-ph/0102074.

[24] W. G. Seligman *et al.*, Phys. Rev. Lett. **79**, 1213 (1997).

[25] G. Moreno *et al.*, Phys. Rev. D **43**, 2815 (1991).

[26] P. L. McGaughey *et al.*, Phys. Rev. D **50**, 2038 (1994).

[27] G. T. Bodwin, Phys. Rev. D **31**, 2616 (1985); **34**, 3932 (1986).

[28] G. T. Bodwin, S. J. Brodsky and G. P. Lepage, Phys. Rev. D **39**, 3287 (1989).

[29] HERMES Collaboration, K. Akerstaff *et al.*, Phys. Rev. Lett. **81**, 5519, (1998).

[30] J. Sterling, Letter to John Peoples, May 1998.

[31] G. David, representing the PHENIX Collaboration, Quark Matter 2001, http://www.rhic.bnl.gov/qm2001/program.html.

[32] D.M. Alde *et al.*, Phys. Rev. Lett. **64**, 2479 (1990).

[33] FNAL E866/NuSea Collaboration, M.A. Vasiliev *et al.*, Phys. Rev. Lett. **83**, 2304 (1999).

[34] S. Gavin and J. Milana, Phys. Rev. Lett. **68**, 1834 (1992).

[35] S.J. Brodsky and P. Hoyer, Phys. Lett. B **298**, 165 (1993).

[36] R. Baier *et al.*, Nucl. Phys. B **484**, 265 (1997); R. Baier *et al.*, Nucl. Phys. B **531**, 403 (1998).

[37] K.J. Eskola, V.J. Kolhinen and P.V. Ruuskanen, Nucl. Phys. B **535**, 351 (1998); K.J. Eskola, V.J. Kolhinen and C.A. Salgado, Eur. Phys. J. C **9**, 61 (1999).

[38] M.B. Johnson, B.Z. Kopeliovich, I.K. Potashnikova, *et al.* (FNAL E772 Collaboration), hep-ex/0010051.

[39] J. Carlson, R. Schiavilla, Rev. Mod. Phys. **70** 743 (1998).

[40] F. Coester private communication; E. T. Berger, F. Coester and R. B. Wiringa, Phys. Rev. **D 29** 398 (1984).

[41] G. E. Brown *et al.*, Nucl. Phys. **A 593** 295 (1995).

[42] H. Jung and G. A. Miller, Phys. Rev. **C 41** 659 (1990).

[43] A. E. L. Diepernik and C. L. Korpa, Phys. Rev. **C 55** 2665 (1997).

[44] V. Papavassiliou, Contribution to the Main Injector Stationary Target Workshop, Fermilab, May 1997.

[45] FNAL E866/NuSea Collaboration, C.N. Brown *et al.*, Phys. Rev. Lett. **86** (2001) 2529; T.H. Chang, Ph.D. Thesis, New Mexico State University, hep-ex/0012034.

[46] FNAL E866/NuSea Collaboration, M.J. Leitch *et al.*, Phys. Rev. Lett. **84**, (2000) 3256; W.M. Lee Ph.D. Thesis Georgia State University.

[47] NA3 Collaboration, J. Badier *et al.*, Z. Phys. **C20**, (1983) 101.

[48] A. Walters, private communication.

[49] C. A. Gagliardi *et al.*, Nucl. Instrum. Methods A **418**, 322 (1998).

[50] P906 Collaboration, D.F. Geesaman *et al.*, *Response to PAC Questions on P906 Proposal for Drell-Yan Measurements of Nucleon and Nuclear Structure with the FNAL Main Injector*, June 10, 1999, (unpublished).

[51] J. M. Jagger and K. M. Thompson, *Cost estimate of P906 magnet.*